TALLINNA TEHNIKAÜLIKOOL
TALLINN UNIVERSITY OF TECHNOLOGY

Faculty of Chemical and Materials Technology

DEVELOPMENT OF Sb_2Se_3THIN FILM SOLAR CELLS BY CLOSE-SPACED SUBLIMATION

Sb_2Se_3 õhukesekileliste päikesepatareide arendamine lähidistants-sublimatsiooni meetodil

MASTER THESIS

Student: Robert Krautmann

Student code 178183KAYM

Supervisor: Dr. Nicolae Spalatu
Dr. Ilona Oja Acik

Tallinn, 2019

(*On the reverse side of title page*)

AUTHOR'S DECLARATION

Hereby I declare, that I have written this thesis independently.
No academic degree has been applied for based on this material. All works, major viewpoints and data of the other authors used in this thesis have been referenced.

"....." ..... 201.....

Author: .....
/signature /

Thesis is in accordance with terms and requirements

"....." ..... 201....

Supervisor: .....
/signature/

Accepted for defence

"....."..... 201... .

Chairman of theses defence commission: .....
/name and signature/

Faculty of Chemical and Materials Technology

THESIS TASK

Student: Robert Krautmann, 178183KAYM

Study programme, Materials and Processes for Sustainable Energetics

main speciality: materials for sustainable energetics

Supervisor(s): Dr. Nicolae Spalatu; Dr. Ilona Oja Acik

Thesis topic:

(in English) DEVELOPMENT of Sb_2Se_3THIN FILM SOLAR CELLS BY CLOSE-SPACED SUBLIMATION

(in Estonian) Sb_2Se_3 õhukesekileliste päikesepatareide arendamine lähidistants-sublimatsiooni meetodil

Thesis main objectives:

1. To familiarise with the CSS method by fabricating Sb_2Se_3 thin films and solar cells
2. To familiarise with CBD and USP deposition methods for depositing CdS and TiO_2 films
3. To acquire knowledge of the main principles of solar cells

Thesis tasks and time schedule:

No	Task description	Deadline
1.		
2.		
3.		

Language: ENG **Deadline for submission of thesis:** "28" May 2019

Student: ……. ..... "....."....201….a

/signature/

Supervisor: …… ..... "....."....201….a

/signature/

Consultant: …… ..... "....."....201….a

/signature/

Terms of thesis closed defence and/or restricted access conditions to be formulated on the reverse side

Contents

PREFACE

The notion of making the following thesis was proposed by Dr. Ilona Oja Acik, the Head of Laboratory of Thin Film Chemical Technologies. Major thesis work was carried out in the Laboratory of Thin Film Chemical Technologies. Throughout the work I was assisted by Dr. Nicolae Spalatu, Dr. Atanas Katerski, Dr. Olga Volobujeva, Dr. Jaan Hiie and PhD student Jako Siim Einsalu. Additionally, I consulted with Dr. Ilona Oja Acik.

My biggest thanks go to Dr. Nicolae Spalatu, who took me under his supervision three months prior to thesis deadline. Being open to discussion and paying attention to every detail, he instilled me confidence we could make our solar cells work. I hope this thesis is a credible final product of the heavy work and long thought we put into these past months.

I would also like to thank Dr. Ilona Oja Acik and the Director of Materials and Environmental Technology Department Dr. Malle Krunks for providing me the opportunity to work on fabricating solar cells, which has been my biggest wish since the day I started working in your laboratory. Your guidance and support have helped me to stay on track and strive towards the desired goal. I am glad to have had the chance work with so many different machines and devices.

I am also thankful to Dr. Atanas Katerski, who was first to give me broader insight into the world of third-generation solar cells. The lengthy discussions we had propelled me to gain deeper understanding of the physics of solar cells.

The study was financially supported by the Estonian Ministry of Education and Research IUT19-4, IUT19-28 and by the European Regional Development Fund project: TK141 Centre of Excellence "Advanced materials and high-technology devices for sustainable energetics, sensorics and nanoelectronics" (1.01.2015−1.03.2023).

Short summary

This master thesis focused on Sb_2Se_3 solar cell fabrication by close-spaced sublimation. I studied the effect of substrate temperature on the film properties and the Sb_2Se_3 solar cell performance. I concluded that highest substrate temperature gave the best Sb_2Se_3 film that also reflected on the best photovoltaic performance. After finding the optimal substrate temperature, I employed three different window layers – sublimated CdS, sprayed TiO_2 and chemically deposited CdS – to study the effect of window layer on the Sb_2Se_3 film properties and the Sb_2Se_3 solar cell performance. TiO_2 proved best partner to Sb_2Se_3 helping to produce Sb_2Se_3 film of highest quality. TiO_2/Sb_2Se_3 solar cell achieved photoconversion efficiency of 3.3%, which was higher than that of the two CdS/Sb_2Se_3 solar cells.

Keywords: Sb_2Se_3 solar cells, close-spaced sublimation, thin film solar cells, ultrasonic spray pyrolysis, chemical bath deposition

List of abbreviations and symbols

PV	Photovoltaics
c-Si	Crystalline silicon
CdTe	Cadmium telluride
CIGS	Cadmium indium gallium selenide
CIS	Cadmium indium diselenide
α-Si	Amorphous silicon
CSS	Close-spaced sublimation
VTD	Vapour transport deposition
GBs	Grain boundaries
DSSC	Dye-sensitised solar cell
HTM	Hole transport material
RTE	Rapid thermal evaporation
PCE	Photoconversion efficiency
CBD	Chemical bath deposition
USP	Ultrasonic spray pyrolysis
CVD	Chemical vapour deposition
PLD	Pulsed laser deposition
ALD	Atomic layer deposition
E_g	Band gap energy
TCO	Transparent conductive oxide
L_d	Minority carrier diffusion length
BSE	Backscattered electrons
SE	Secondary electrons
SEM	Scanning electron microscopy
EDX	Energy-dispersive X-ray spectroscopy
XRD	X-ray diffraction
EQE	External quantum efficiency
J_{SC}	Short circuit current density
V_{OC}	Open circuit voltage

INTRODUCTION

Photovoltaics (PV), converting sunlight to electricity, stands as one of the most promising renewable technologies to help fulfil increasing global energy demand and tackle global warming. International Renewable Energy Agency (IRENA) states that the share of renewable energy in electricity generation must reach 86% by 2050 to keep the global temperature rise below 2°C, the target set in the Paris Agreement [1] [2]. Today, solar PV accounts for around 2% of total world electricity generation with cumulative capacity of around 400 GW [3]. Meeting the aims of the Paris Agreement would require the installed solar PV capacity to exceed 8 500 GW in 2050 [2]. Over the past decade, prices of solar panels have reduced significantly, but there has been a lack of substantial improvement in the standard silicon panels [4]. However, further reductions in the cost of solar panels by a factor of 2-5 are required to increase competitiveness of solar PV in the energy market [5]. At present, crystalline silicon (c-Si) panels make up 90% of the global PV market [6]. This illustrates why there is an ongoing search for new materials that could potentially lead to the commercialisation of more efficient and cost-effective solar panels and would thereby accelerate the energy transition towards renewables. Higher efficiency in solar cells results from more light being harvested. Cost-effectiveness can be achieved by reducing solar panel cost but retaining the former efficiency. Therefore, solar cell technologies, which offer less expensive manufacturing costs, such as thin film and perovskite solar cells, have huge potential to challenge crystalline silicon in the coming decades.

Thin film solar cell technologies employ materials, which are low cost, non-toxic, robust and stable [7]. Suitable materials possess high absorption coefficient and direct band gap, which allows strong light absorption at reduced thicknesses. Thin films have thicknesses usually in the range of 1-5 µm and they can be deposited on cheap module-sized substrates such as glass, plastic or stainless steel [5]. In contrast, c-Si solar panels employ a 180-300 µm thick Si wafer to capture 95% of incident light, which ultimately accounts for approximately 52% of the solar panel price [5] [7] [8]. At present, solar cells based on cadmium telluride (CdTe), copper indium gallium selenide (CIGS), copper indium diselenide (CIS), and amorphous silicon (α-Si) have been most widely investigated. To date, CdTe and CIGS solar cells have been most successful in achieving efficiencies of 20.4% and 20.8%, respectively [9]. Moreover, CdTe solar cells make up 5% of the solar PV market [6]. Its commercial success stems from low cost manufacturing processes. Material properties, such as high vapour pressure, binary structure and high chemical stability, enable CdTe to be grown using methods like vapour transport deposition (VTD), close-spaced sublimation (CSS) [10]. But despite successful deployment of CdTe and CIGS solar cells, the toxicity of elements Cd, the scarcity of In and Te, and high price of In and Ga, hinder the scaling up of CdTe

and CIGS solar cells production [9]. Therefore, there is a huge interest in finding non-toxic and low-cost photovoltaic materials, potentially adapting to the already established fabrication methods.

This thesis work focused on the development of Sb_2Se_3 solar cells by close-spaced sublimation (CSS). Sb_2Se_3 is an emerging photovoltaic absorber material, which exhibits suitable optoelectronic properties and is compatible with the fabrication of CdTe photovoltaics. CSS is a promising deposition technique for growing polycrystalline Sb_2Se_3 films, because it can yield large grains that have preferred orientation and low density of grain boundaries [11]. Crystal growth of polycrystalline thin films depend on multiple parameters, such as (1) evaporation temperature, (2) inert gas pressure, (3) distance between the source and the substrate, and (4) substrate temperature [12]. Herein, we investigated the effect of substrate temperature on the Sb_2Se_3 film properties and the Sb_2Se_3 solar cell performance. Sb_2Se_3 films were deposited at substrate temperatures of 300 to 450 °C. We also studied the effect of window layer on the Sb_2Se_3 film properties and the Sb_2Se_3 solar cell performance. Altogether, we had three different window layers – sublimated CdS, sprayed TiO_2 and chemically deposited CdS – partnering the Sb_2Se_3 absorber.

In the following thesis work, I will first give a theoretical background of the Sb_2Se_3 solar cells, the physics of solar cells, implemented deposition methods and characterisation techniques. This is followed by the experimental. Herein, we fabricated Sb_2Se_3 solar cells. TiO_2 window layer was deposited by ultrasonic spray pyrolysis (USP) and CdS window layers were deposited using either close-spaced sublimation (CSS-CdS) or chemical bath deposition (CBD-CdS). Sb_2Se_3 films were deposited by CSS. Material characterisation techniques included scanning electron microscopy (SEM), energy-dispersive X-ray spectroscopy (EDX), X-ray diffraction (XRD), UV-vis-NIR spectrophotometry and van der Pauw measurement. Sb_2Se_3 solar cells were measured by current- voltage (J-V) characteristic and external quantum efficiency (EQE).

1. THEORETICAL BACKGROUND

1.1 Sb_2Se_3 solar cells

1.1.1 Sb_2Se_3 as an attractive photovoltaic absorber material

Antimony selenide (Sb_2Se_3) has emerged as a potential alternative to CdTe because of its attractive properties, such as optical band gap of 1.1–1.3 eV [9] and high absorption coefficient (> 10^5 cm^{-1}) [13]. Sb_2Se_3 is naturally a p-type material like CdTe [14]. Furthermore, Sb and Se are highly abundant [9]. Sb_2Se_3 is a non-toxic binary compound with single phase and fixed composition [9] [15], also exhibiting low melting point of 608 °C [16] [17] and high vapour pressure (~1200 Pa at 550 °C) [12] [17]. Altogether, it renders Sb_2Se_3 compatible with low temperature vacuum-based deposition techniques already applied for CdTe photovoltaics [12]. Another exciting feature of Sb_2Se_3 lies in its one-dimensional (1D) crystal structure [13]. Sb_2Se_3 crystals are composed of $(Sb_4Se_6)_n$ ribbon-like units stacking along the c-axis, in the [001] crystal direction, resulting in highly anisotropic properties [17]. While strong covalent bonds between Sb-Se form in the [001] direction, neighbouring units only bond through weak van der Waals forces in the [100]- and [010]- direction [13]. Interestingly, Van der Waals interactions avoid the formation of dangling bonds at the grain boundaries (GBs), which is the main cause for non-radiative recombination losses that often limit the performance of polycrystalline PV materials [18]. Figure 1 compares the grain boundaries of CdTe and Sb_2Se_3, demonstrating how directional growth of Sb_2Se_3 terminates the GBs free of dangling bonds [13].

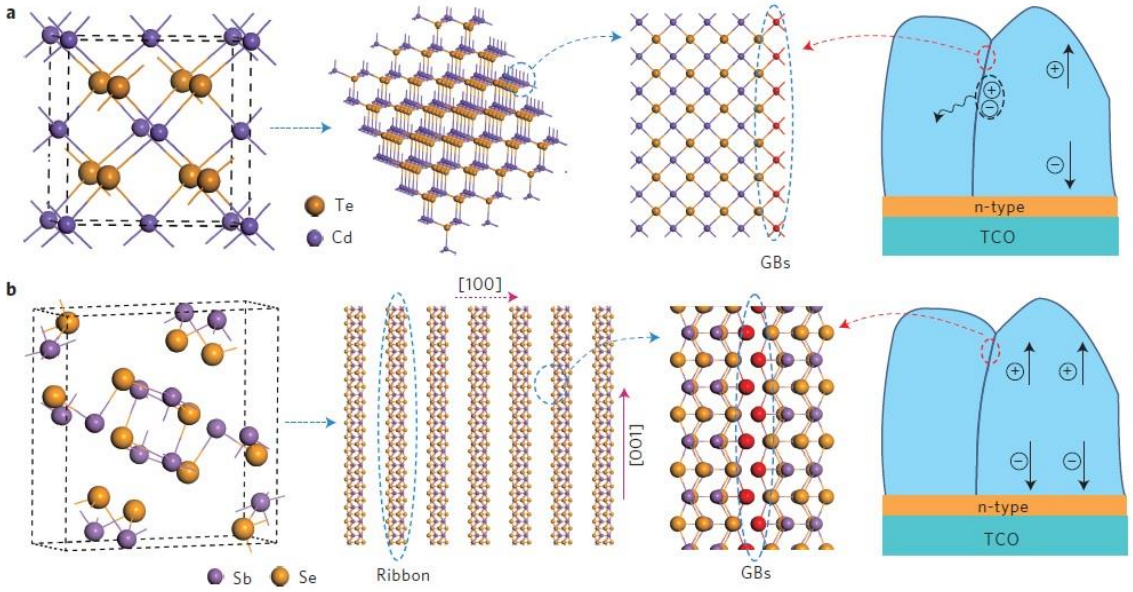

Fig. 1. (a) CdTe crystal grows in 3D, thus giving rise to dangling bonds at the GBs, which act as potential recombination centres. (b) Sb_2Se_3 grains grows in [001]-crystal direction, forming vertically stacked ribbons, in which all atoms are bound, thus the GBs are free of dangling bonds [17].

As for Sb_2Se_3, directional growth also affects the carrier transport. It is easier for minority carriers to travel across the ribbon than to hop between ribbons [17]. Chen et al. demonstrated greater hole mobilities in the [221]-direction compared to the [020]- and [120]-directions (2.59, 1.17 and 0.29 $cm^2 V^{-1} s^{-2}$, respectively) [19]. Hence, Sb_2Se_3 ribbons that are either vertical or slightly tilted (with an angle to the normal of the substrate surface) offer better pathways for carrier transport.

1.1.2 State-of-the-art Sb_2Se_3 photovoltaic devices over time

Photovoltaic device successfully employing Sb_2Se_3 absorber was first realised in 2009, achieving 0.66% efficiency [20]. Thereafter, Sb_2Se_3 solar cells have undergone rapid improvement. In 2013, Choi et al. reported a 3.2%-efficient Sb_2Se_3 solar cell that employed spin-coated Sb_2Se_3 as a light sensitizer on mesoporous titania (TiO_2), thus replicating dye-sensitized solar cell (DSSC) configuration [21]. In 2015, Zhou. et al. demonstrated a CdS/Sb_2Se_3 solar cell with photoconversion efficiency (PCE) of 5.6% [17]. In 2017, Wang et al. achieved 6%-efficient solar cell with ZnO/Sb_2Se_3 superstrate configuration [22]. Same year, Chen et al. employed colloidal PbS film as hole transport material (HTM) on the Sb_2Se_3 absorber, attaining PCE of 6.5% with $CdS/Sb_2Se_3/PbS$ superstrate configuration [23]. In previous three studies, Sb_2Se_3 film was grown by rapid thermal evaporation (RTE) with growth rate (1 µm min^{-1}), which is comparable to close-spaced sublimation (CSS) (1– 5 µm min^{-1}) [10] [17]. In 2018, Hutter et al. reported a 6.6%-efficient superstrate TiO_2/Sb_2Se_3/PCDTBT solar cell, where Sb_2Se_3 was deposited by CSS [11]. Same year, Wen et al. obtained champion solar cell for superstrate CdS/Sb_2Se_3 solar cell with PCE of 7.6% [12]. Sb_2Se_3 was deposited by vapour transport deposition (VTD) that is the prevalent commercial technique used for CdTe solar cells [10]. In 2019, Phillips et al. obtained PCE of 5.5% for a TiO_2/Sb_2Se_3 superstrate configuration, with Sb_2Se_3 grown via CSS [18]. Most notably, Li et al. achieved record PCE of 9.2% with substrate $ZnO:Al/ZnO/CdS/TiO_2/Sb_2Se_3/MoSe_2$/Mo solar cell. Whilst previous solar cells had Sb_2Se_3 grains growing preferably in the [211]- and [221]-direction [11] [12] [17] [18] [22] [23], Li et al. were first to demonstrate ribbons that were completely upright, parallel to the c-axis [13].

1.1.3 Putting Sb_2Se_3 solar cells into our perspective

Given our lab experience with fabricating superstrate CdS/CdTe solar cells and superstrate TiO_2/Sb_2S_3/P3HT solar cells, we took the configurations of the 7.6%-efficient superstrate CdS/Sb_2Sb_3 and the 5.5%-efficient TiO_2/Sb_2Se_3 [18] as the state-of-the-art reference. Figure 2 displays the Wen et al. fabricated superstrate CdS/Sb_2Sb_3 solar cell that comprises of front contact indium-doped tin oxide (ITO), window layer cadmium sulfide (CdS), absorber layer Sb_2Se_3 and back contact gold (Au) [12]. They deposited cadmium sulfide (CdS) window layer by CBD onto glass/ITO substrate, followed

by the deposition of the Sb_2Se_3 absorber by VTD. Lastly, Au was thermally evaporated onto the Sb_2Se_3 as a back contact and additionally onto bare glass/ITO. [12]

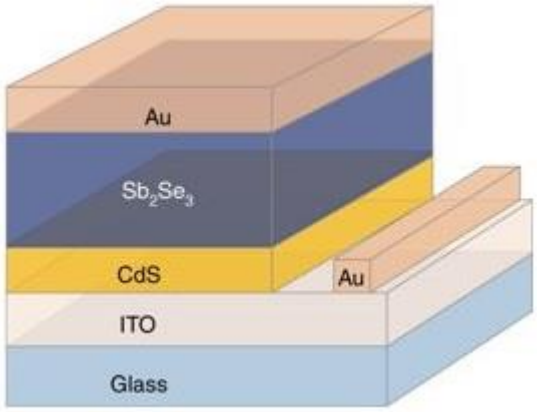

Fig. 2. Superstrate configuration of CdS/Sb_2Se_3 solar cell [12]

Figure 3 shows Phillips et al. fabricated superstrate TiO_2/Sb_2Se_3 solar cell that comprises front contact fluorine-doped tin oxide (FTO), window layer titanium dioxide (TiO_2), absorber layer Sb_2Se_3 and back contact gold (Au) [18]. They deposited TiO_2 window layer by spin-coating onto glass/FTO substrate , followed by the deposition of the Sb_2Se_3 absorber by CSS and thermal evaporation of Au back contact [18].

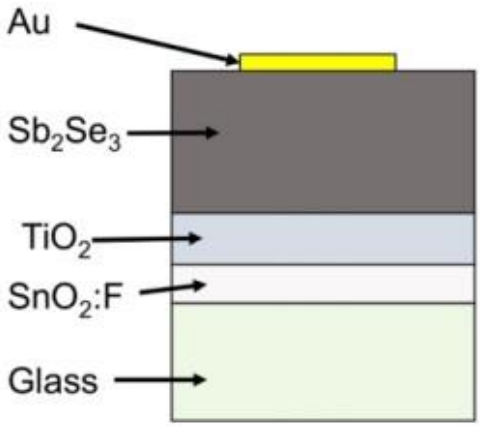

Fig. 3. Superstrate configuration of TiO_2/Sb_2Se_3 solar cell [18]

Wen et al. and Philips et al. achieved optimal PV performance, when substrate temperature was set to 390 °C [12] and 450 °C [18], respectively. In that case, Sb_2Se_3 grains were found growing preferably in the [211]- and [221]-direction, which is considered beneficial for carrier transport [12] [17] [18] [22]. Figure 4 exemplifies the [211]- and the [221]-direction, along which carriers possess longer diffusion lengths, thereby improving charge separation [19] [24].

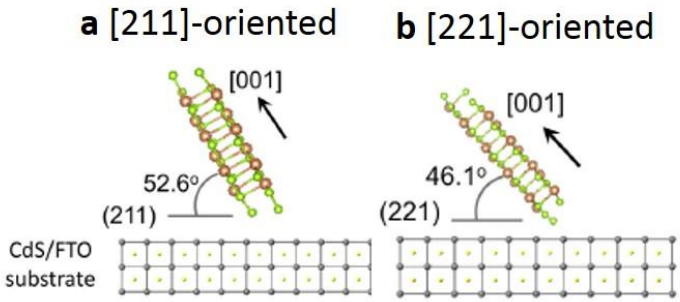

Fig. 4. (a) [211]-oriented Sb_2Se_3 crystal grains inclined at an angle of 52.6° and(b) [221]-oriented Sb_2Se_3 crystal grains inclined at an angle of 52.6° to the [001] crystal direction (c-axis) [24]

1.1.4 CdS window layer

Cadmium sulphide (CdS) is a wide band gap semiconductor, exhibiting direct band gap E_g of approximately 2.5 eV and high transparency (> 80%) [25]. It has two crystal phases: cubic zinc blende with preferred orientation in the [111]-direction and hexagonal wurtzite with preferred orientation in the [002]-direction [26]. Besides successful deployment in CdTe and CIGS solar cells, where n-type CdS partners p-type CdTe/CIGS [6], CdS films have also been applied in other optoelectronic devices, such as optical sensors [27], light-emitting diodes [28] and transistors [29]. In CdTe solar cells, the CdS window layer has proved successful due to ion diffusion and subsequent intermixing of sulfide and telluride, resulting in a CdSTe alloy film forming at the interface, which reduces interfacial recombination and thus improves the PV performance [6]. For solar PV, CdS window layers have mainly been grown via vapour transport deposition (VTD) [6], close-spaced sublimation (CSS) [10], and chemical bath deposition (CBD) [12], of which CBD is the most widely used owing to its simplicity and low cost. However, due to high toxicity of Cd in CdS [11], low-toxicity window materials of comparable quality are sought.

1.1.5 TiO_2 window layer

Titanium dioxide (TiO_2) is considered a viable alternative to CdS mainly due to its larger band gap (E_g = 2.8–3.3 eV) [30], higher optical transmittance and superior chemical stability [18]. Anatase and rutile, both having tetragonal structure, are the prevalent crystal phases, of which anatase possesses more suitable optoelectronic properties [30]. Main crystal phases of anatase and rutile are (101) and (110), respectively [31].Titania can be produced by numerous techniques, such as vacuum-based sputtering, pulsed laser deposition (PLD), chemical vapour deposition (CVD), atomic layer deposition (ALD) and solution-based techniques, such as sol-gel, spray pyrolysis, and spin coating [30]. Different techniques enable TiO_2 to be developed in either planar, mesoporous, nanoparticle, or nanostructured form. This explains its extensive employment as either photoanode

or electron transport layer (ETL) in hybrid [32], perovskite [33] and dye-sensitized solar cells [34]. For instance, perovskite solar cells are deposited onto the mesoporous titania, because it forms a highly porous scaffold of adjoined nanoparticles, thus offering large contact area with the perovskite for efficient photocarrier separation [35]. In addition to solar cells, TiO_2 has been used in photocatalytic applications [36], gas sensors [37], photonics [38] and air purifiers [39].

1.2 Physics of solar cells

Solar cell is a photovoltaic device, which produces electrical energy under illumination. Photovoltaic devices incorporate semiconductors, which exhibit suitable band gap for photon absorption and the consequent electron-hole (e-h) pair generation. Two adjoined semiconductors of p- and n-type conductivity establish p-n junction that separates the charges, thus enabling photocurrent flow and photovoltage generation.

1.2.1 Thin film solar cell configuration

Typical thin-film solar cell comprises of absorber layer and window layer sandwiched between front and back contact. Front contact and window layer should be transparent to large portion of incident sunlight. Front contact is typically a transparent conductive oxide (TCO) film deposited onto glass substrate. In general, thin film solar cells employ either indium-doped tin oxide (ITO) or fluorine-doped tin oxide (FTO). Their high transparency (>80%) and low sheet resistance (<30 Ω/sq) allows for efficient extraction of charges into the external circuit [10]. Window layer is usually an n-type wide-bandgap semiconductor material, which is transparent to visible light photons. Window layer can participate in the e-h pair generation but is rather used to establishing p-n junction, also known as depletion region, with the absorber material and reducing lattice mismatch between the front contact and the absorber. Widely used window layers include CdS, TiO_2 and ZnO. Absorber layer is responsible for photocarrier generation and charge separation via the depletion region formed at the interface of window and absorber layers. Most widely explored absorber materials for thin film solar cells are CdTe, CIGS, CIS and α-Si [6]. Back contact is made of metal, such as gold (Au), copper (Cu), or molybdenum (Mo) that possess very high conductivity and can form ohmic contact with the back of the absorber [25]. Metal contacts also assist in charge extraction into external load. Considering material peculiarities, thin film solar cells can be fabricated in two configurations. In a superstrate configuration, as shown in Fig. 5a, CdS/CdTe solar cell is gradually stacked onto the TCO/glass substrate [40]. As for substrate configuration, as shown in Fig. 5b, deposition sequence is in reverse with back contact serving as the base.

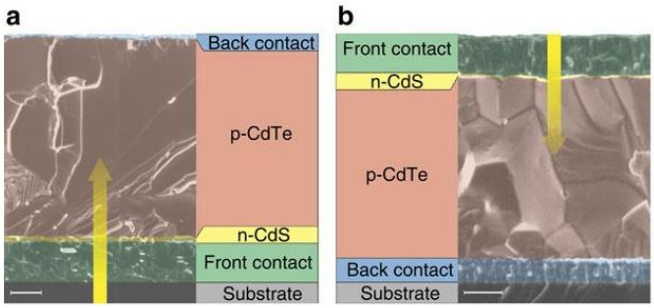

Fig. 5. Schematic of (a) superstrate configuration and (b) substrate configuration of CdS/CdTe solar cell. Yellow arrow shows from which side light enters the structure. [40]

1.2.2 Formation of p-n junction

p-n junction materials

Establishing p-n junction requires combining p-type semiconductor material with n-type semiconductor material. P-type semiconductor has excess of holes, n-type semiconductor has excess of electrons. In c-Si solar cells, n-type and p-type Si are obtained via doping. Si is intrinsically neutral, yet becomes p-type, when it is doped with an acceptor atom, such as boron (B) (group III), which has one valence electron less (3 e^-) than Si (4 e^-). Contrarily, Si becomes n-type, when it is doped with a donor atom, such as P or As (group V), which has one additional electron (5 e^-) than Si (4 e^-), as shown in Figure 6. Consequently, p-n junction is formed within single material, thus it is called a homojunction. [41]

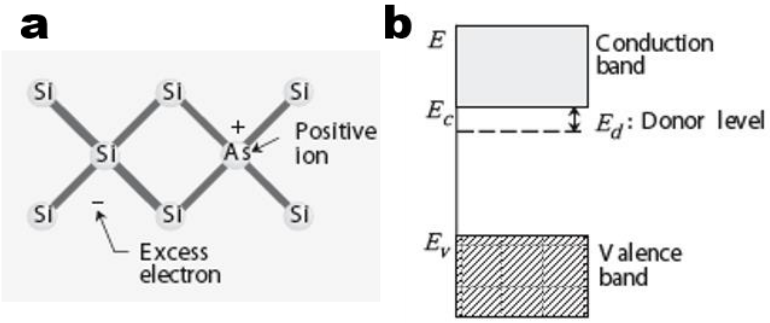

Fig. 6. (a) Schematic of doping Si with As (group V) dopant. (b) As donates one electron to the conduction band, produce n-type silicon with Fermi level close to the conduction band. [41]

As for thin film solar cells, materials that exhibit intrinsic n- or p-type conductivity are in huge demand, because they do not require additional doping [42]. In case of CdS/CdTe, where CdS and CdTe form a heterojunction, CdS is intrinsically n-type due to sulfur vacancies (V_S) [26], whilst CdTe becomes p-type due to cadmium vacancies (V_{Cd}) [10]. Similarly, heterojunction is formed between TiO_2 and Sb_2Se_3, where TiO_2 is n-type due to oxygen vacancies (V_O) [43] and Sb_2Se_3 is p-type due to antimony vacancies (V_{Sb}) and selenide antisite defects (Se_{Sb}) [12].

Establishing electric field

When p-type and n-type material are brought together, there is diffusion of majority carriers, as shown in Figure 7. In p-type material with holes (h^+) being the majority carriers, holes diffuse down its concentration gradient into n-type material, leaving behind negatively-charged ionised acceptor atoms. In n-type material with electrons (e^-) being the majority carriers, electrons diffuse down its concentration gradient into p-type material, leaving behind positively-charged ionised dopant atoms. [41] As a result, space-charge region is formed with a "built-in" electric field, as shown in Fig. 7. This electric field causes drift current of minority carriers (e^- in p-type and h^+ in n-type), which opposes the diffusion current of majority carriers. Therefore, junction acts as an electrostatic potential barrier to diffusion current and low resistance path to desired drift current [7].

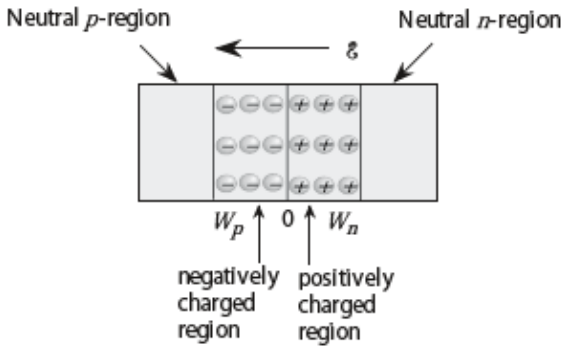

Fig. 7. Diffusion of majority carriers leads to the formation of neutral and depletion areas. ξ marks the direction of the electric field. [41]

Eventually comes a point of equilibrium, where diffusion and drift currents cancel each other out with the junction region being completely depleted of minority carriers, as shown in Figure 8. Under equilibrium condition, the Fermi energies, which mark the highest occupied energy state at 0 K for both p and n side, align across the junction. This causes band bending only within the depletion region, as shown in Fig. 8, whereas neutral p and n regions remain flat [41].

Depletion width

The depletion region extends a distance W_p in the *p*-type and a W_n distance in the n-type, as shown in Fig. 8. Depletion widths W_p and W_n are related to acceptor N_A and donor N_D densities, respectively, which also relate to the impurity concentration [41]. In case of silicon and thin film solar cells, e-h pair generation does mainly occur in the base and the absorber, respectively. Therefore, it is desired that the depletion region extends further in the *p*-type absorber, where the photocarriers are generated [7]. Provided that the n-type impurity concentration is significantly larger to that of *p*-type ($N_D \gg N_A$), the depletion width of W_n will become much smaller than the

W_p [44]. Thus, although a very strong field exists over a very narrow region in the *n*-side, the depletion region exists primarily on the lightly doped side [41].

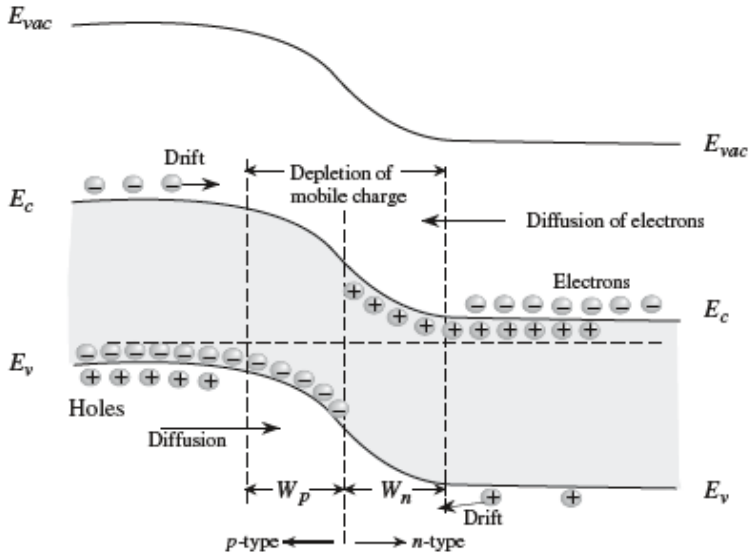

Fig. 8. Schematic of a p-n junction. Fermi levels align under thermal equilibrium. Positive space charge at the n-type has lower electrostatic potential, thus causing band bending relative to negative space charge at p-type. Electric field is therefore confined to depletion region. [41]

Figure 9 illustrates the depletion width dependence on the dopant densities. This describes the abrupt p^+-*n* junction, where $N_A \gg N_D$, thus being the exact opposite to the junction desired in thin film solar cells. Doping density of *p*-type is much larger at the interface of two materials, as shown in Fig. 9a, therefore the depletion width is smaller, resulting in a stronger electric field from $-W_p$ to 0, as seen in Fig. 9b. Contrarily, donor density of *n*-type is much smaller, hence resulting in a larger depletion width. Despite less strong electric field, more photocarriers can be potentially collected.

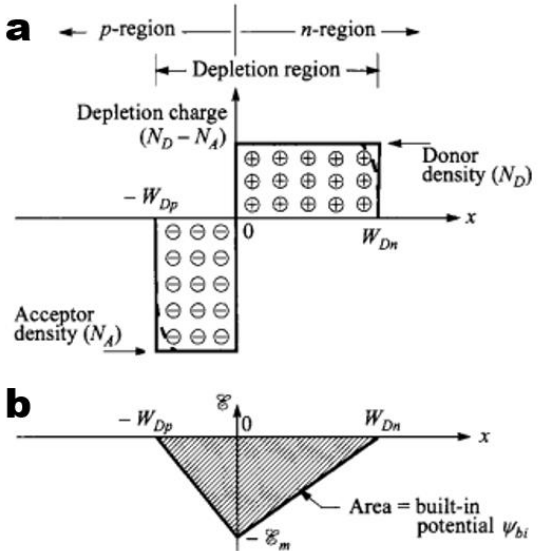

Fig. 9. Schematic of relationship between (a) doping density and depletion width, and (b) doping density and the electric field [44]

1.2.3 Photocurrent generation and collection

Generated photocurrent is a balance between light absorption, charge generation and charge recombination [1]. Following paragraphs describe shortly the underlying mechanisms.

Light absorption

Solar cell absorbs light photons that have energy equal or above than that of band gap energy E_g of the absorber material. Photons, which have energy below semiconductor band gap energy ($\hbar\omega < E_g$), cannot generate photocarriers, and they either reflect or pass through. The probability of semiconductor material absorbing a photon of energy $\hbar\omega$ is characterised by absorption coefficient $\alpha(\hbar\omega)$, which is an intrinsic material property [45]. Absorption coefficient shows how well does material absorb a photon of given energy. Figure 10 depicts the absorption coefficient

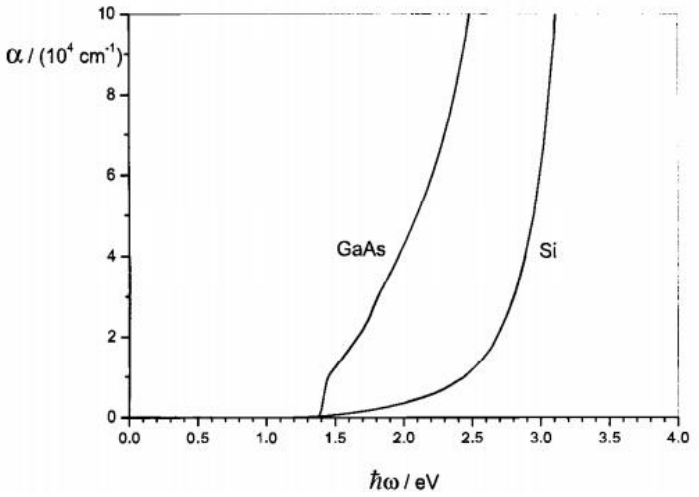

Fig. 10. Absorption coefficient α of "direct" GaAs and "indirect" Si semiconductor [45].

functions of GaAs and Si semiconductor materials. It exemplifies the dependence of absorption coefficient upon the photon energy. Moreover, it reveals whether semiconductor has direct or indirect optical band gap. GaAs has sharp absorption edge in the visible light region, as shown in Fig. 10, thus it exhibits a direct optical band. On the other hand, Si absorption coefficient function follows exponential growth in the visible light region, hence having an indirect band gap.

Overall, higher the absorption coefficient, less material is needed for absorption. Thickness required for complete light absorption can be deduced from Beer-Lambert law, as shown in Equation 1.

$$\frac{I}{I_0} = e^{-\alpha t} \tag{1}$$

where I is the light intensity after travelling distance t (in cm) within the material, I_0 is the initial light intensity, and α is the absorption coefficient in cm^{-1} [7].

Photocarrier generation and charge separation

When a semiconductor absorbs a photon of energy $\hbar\omega \geq E_g$ it generates the e-h pair. Electron is promoted to the conduction band, whereas hole into valence band, as shown in Figure 11.

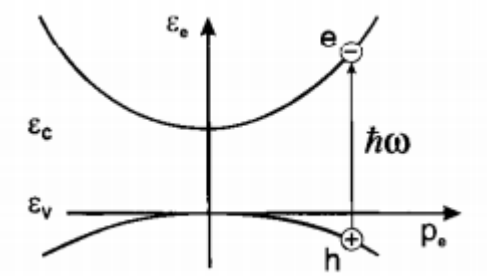

Fig. 11. Promotion of electron into conduction band (ε_c) and hole into valence band (ε_V) by the absorption of photon with energy $\hbar\omega > E_g$ [45]

When the photocarriers are generated in the depletion region, electric field sweeps the electrons into n-type and holes into p-type. If the e-h pair is generated in either p- or n-region, minority carrier must reach the depletion region to be separated from the majority carrier. Figure 12 depicts the carrier diffusion of electrons from the region where e-h pair was generated to the depletion region. Electrons that are generated more than diffusion length L_d away from the depletion region are lost to recombination, as shown in Fig. 12. Electron that is within the L_d is separated from the hole at the junction and can therefore be collected. [5]

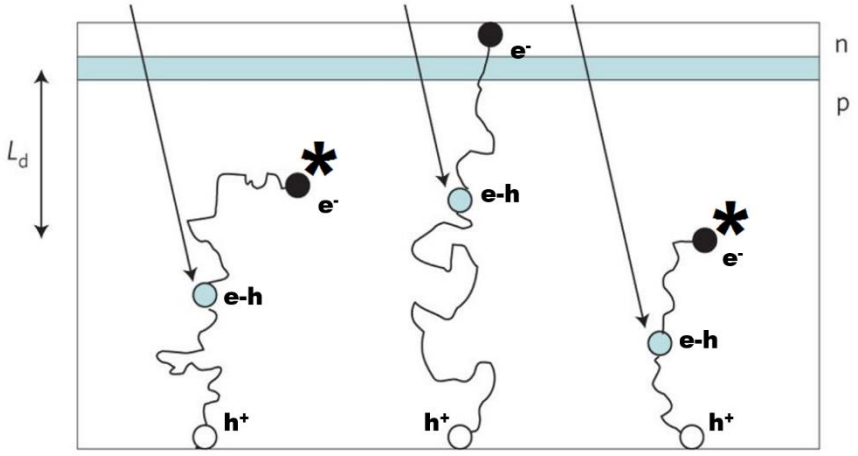

Fig. 12. Minority carrier diffusion to the depletion region. Electrons indicated by asterisk do not make it to the depletion region, because the e-h pairs were generated more than L_d from the depletion region. E-h pair generated less than $L_d$away from the junction allows the electron to be successfully separated at the depletion region. [5]

Diffusion length is the distance minority carrier can travel before it recombines with the majority carrier. Therefore, it plays a key role in choosing the optimal absorber thickness. c-Si has electron diffusion length L_e of ~180 µm, which renders absorber thicknesses thicker than the L_e simply redundant, as shown in Fig. 12. So far, diffusion length of electrons in the Sb_2Se_3 solar cells has been

found to be in the range of 0.3 and 1.7 µm, also showing dependence on the direction of the Sb_2Se_3 crystal growth [19].

Photocarrier recombination

Recombination is the reverse process to the generation of electrons and holes. When electrons and holes recombine, they annihilate and cannot generate photocurrent. There are four main recombination processes, namely radiative recombination, Shockley Read Hall (SRH) recombination, Auger recombination, and surface recombination, as shown in Figure 13a, b, c and 14, respectively [7]. Radiative recombination is a process, where the electron relaxes and recombines with the hole, causing emission of a photon, as shown in Fig. 13a [45]. Radiative emission is more prevalent in direct band gap semiconductors, especially at photon energies that are closer to the band gap energy [7]. Auger recombination is a process, where there is a collision of two minority carriers of the same type, causing one carrier to recombine and give up the released energy to the other carrier, as shown in Fig. 13c. Auger processes occur mainly in highly doped and low band gap materials, but also at high temperature Radiative and Auger recombination are deemed unavoidable, because they are part of the intrinsic material behaviour [7].

On the contrary, Shockley Read Hall (SRH) and surface recombination can be reduced, as they stem directly from the quality of material. SRH recombination is the predominant recombination mechanism where impurities introduce forbidden energy states to the band gap [7]. Impurities can either be point defects, such as vacancies, or impurity atoms, such as extrinsic impurities, which are localised in the crystal lattice. It is important to note that whilst shallow impurities serve as dopants, deeper impurities produce trap states and recombination centres. Trap states typically hold onto a single carrier, which enables it to be released by thermal activation. However, if the next capture occurs before the release of the first carrier, the e-h pair will annihilate, as shown In Fig. 13b [7].

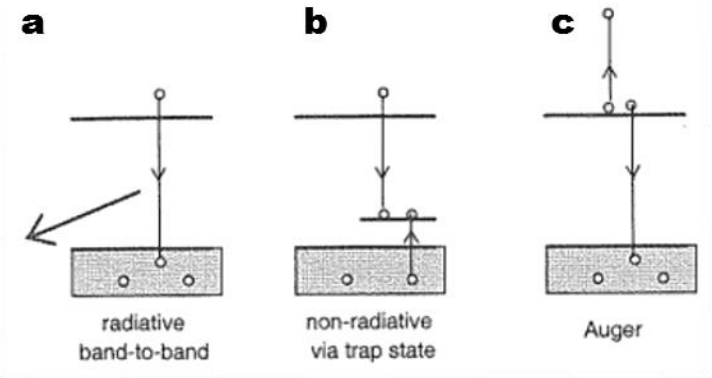

Fig. 13. Schematic of recombination processes. (a) Radiative recombination, (b) SRH recombination, and (c) Auger recombination [7]

Recombination centres are energy states that lie deeper, closer to the centre of the band gap. These states have equal susceptibility to both types of carriers, thus providing largest contribution to recombination. SRH recombination is most effective in the case where n and p densities are of same magnitude, namely in intrinsically neutral regions. SRH processes can therefore be suppressed, when one type of carrier is increased by orders of magnitude. [7] [45]

In this study, surface recombination is of paramount importance due to the presence of high density of grain boundaries and heterojunction interface between two semiconductors. Like trap states, surface and interface states are localised in the lattice, capable of trapping charge and bring forth recombination. Lattice dislocations, interstitials, and vacancies may give rise to gain boundaries that act as potent recombination centres. In addition, dangling bonds and extrinsic impurities at the interface create trap states that impedes charge transport. [7] Figure 14 shows that these surface states have continuous energy levels in the otherwise forbidden band gap [45].

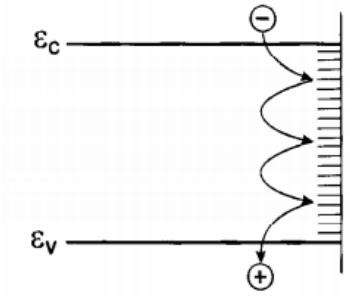

Fig. 14. Schematic shows continuous energy level distribution for surface defect states in the forbidden band gap region between the conduction ε_C and the valence ε_V band [45]

At the grain boundaries, the surface states are filled up by the majority carriers, just like in the case of junction formation between two semiconductors. A depletion region is formed between the boundary, at which the trapped majority carriers accumulate space charge, and the semiconductor, which is depleted of charge near the grain boundary. Figure 15 illustrates the formation of depletion region at the grain boundary of n-type semiconductor. Accumulation of electrons at the surface states gives rise to depletion of majority carriers and produces an electric field. This acts as a

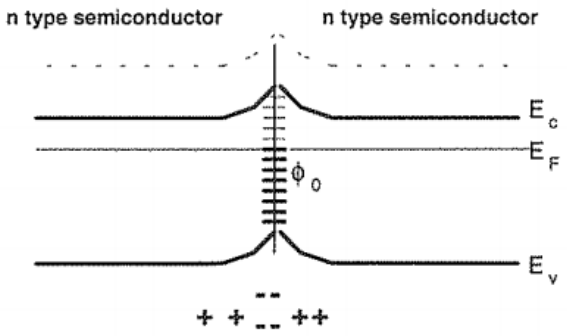

Fig. 15. Schematic of surface states at grain boundaries forming an electric field, which pulls the minority carriers to surface states, therefore causing recombination. [7]

potential well to the minority carriers of opposite charge, consequently causing recombination [7]. Similarly, at the interfaces of two semiconductors, charged trap states introduce discontinuities to the band bending, hence impeding charge transport and increasing recombination [45].

Extraction of charges

In case of thin film solar cells employing a heterojunction of two semiconductors, TCO front contact and Au back contact are deployed to assist the extraction of photocarriers into the external circuit. Metal contact is defined by the work function φ, which is the absolute value of chemical potential of its electrons [45]. When metal and semiconductor are brought together, depletion region occurs, as was shown in Fig. 8. Metal has high concentration of electrons; therefore, depletion region is confined to the semiconductor. Low-resistance charge transport requires ohmic contact. Figure 16 illustrates the formation of ohmic contact between n-type semiconductor and metal. Metal has a lower work function compared to the n-type semiconductor. Hence, upon contact, this causes the accumulation of electrons at the semiconductor-metal interface, which facilitates the charge transport of electrons. Contrarily, p-type semiconductor makes a good ohmic contact with a metal having large work function. [45]

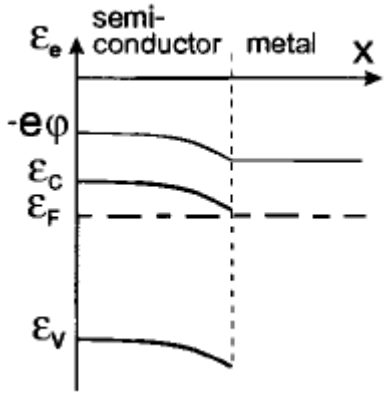

Fig. 16 Schematic of the ohmic contact between n-type semiconductor and metal. Smaller work function allows the accumulation of electrons at the vicinity of metal surface. [45]

Metal-semiconductor interface does also accommodate high concentration of interfacial trap states. Holes that are generated in the absorber can undergo capture by the defect states that lie close to the Fermi level of the metal . Back surface recombination can be reduced through heavy doping of the vicinity of the semiconductor-metal interface [45]. In this case, Fermi level of the semiconductor moves closer to the valence band, thus saturating the defect states. [7]

1.3 Thin film deposition methods

1.3.1 Close-spaced sublimation (CSS)

Close-spaced sublimation (CSS) is an evaporation technique for depositing solid thin films. Solid source material is heated up to the point of vaporisation. Vapour particles travel onto target substrate along the diffusion gradient, eventually condensing onto substrate, which is at lower temperature [10]. Deposition is carried out in high vacuum to prevent contamination and allow only source vapour particles to traverse directly onto the target substrate.

Closed-spaced sublimation system is depicted in Figure 7. Before deposition, reaction chamber is evacuated to attain high vacuum. First, rotary oil pump is used to achieve vacuum levels of 10^{-4} Torr. Then, additional diffusion pump is used to achieve high vacuum of 10^{-6} Torr. Evaporation of source material takes place in a closed chamber, where substrate is facing the source material at the distance of about 11 mm. Source and target are both equipped with a heating filament made of tungsten. Reaction chamber walls are covered with quartz to avoid contamination from graphite at elevated temperatures [10]. During the deposition, source material is heated up to the temperature at which solid source material undergoes sublimation. At the same time, target substrate is also heated up, but left at a lower temperature, which would allow for the condensation of vapour particles on the substrate surface. Temperatures of source and target are monitored by thermocouples. Crystallinity of the thin films depends on the distance between the source and substrate, evaporation and substrate temperature, and background gas pressure [12]. Background gas pressure is applied by inert gas, which can improve the uniformity of thin film by lowering the kinetic energy of vapour particles [12] [17]. This system, however, does not have gas inlet.

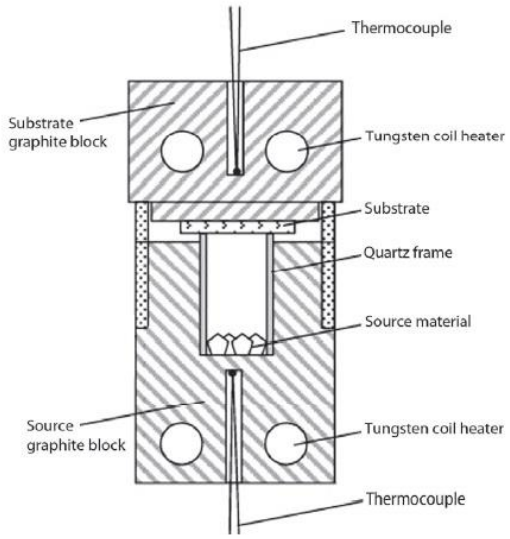

Fig. 7. Schematic diagram of close-spaced sublimation reaction chamber [10]

1.3.2 Ultrasonic spray pyrolysis (USP)

Ultrasonic spray pyrolysis (USP) is a simple solution-based technique for fast and low-cost thin film deposition [46]. Precursor solution is nebulised by ultrasonication and then guided onto a hot plate to deposit metal oxide thin films [47]. Carrier gas, such as compressed air, is used to assist material transfer to the substrate. Upon reaching the substrate surface, solvent evaporates, leading the desired precursor to thermally decompose into a stable product [47].

Figure 8 depicts the experimental setup for ultrasonic spray pyrolysis. Precursor solution is placed into a closed chamber of the ultrasonic nebuliser, where it undergoes ultrasonication to vaporise the solution into fine droplets [48]. In the nebuliser piezo crystals oscillate at high frequency, thus making stationary waves inside the precursor solution and giving rise to rapid vaporisation [49]. Higher oscillation frequency results in finer droplets. Depositing finer droplets results in more homogenous film with smoother surface [49] [50]. The precursor vapour is subsequently guided onto the heat plate with the aid of transport gas. At the nozzle, complementary director gas is used to aim the precursor vapour onto the substrate surface. Substrate is heated up by the hot plate set to the temperature desired for the thin film deposition. During the deposition, nozzle follows a pre-programmed raster to ensure homogenous film coverage.

Although simple, there are number of factors affecting the film growth and properties. Spray rate, substrate temperature, ambient pressure, transport and director gas flow rate, exposure of substrate are the main critical factors for successful deposition [51]. Furthermore, concentration of precursor solution, droplet size and evaporation rate of solvent determine the thickness and crystallinity of the deposited thin film [51] [52].

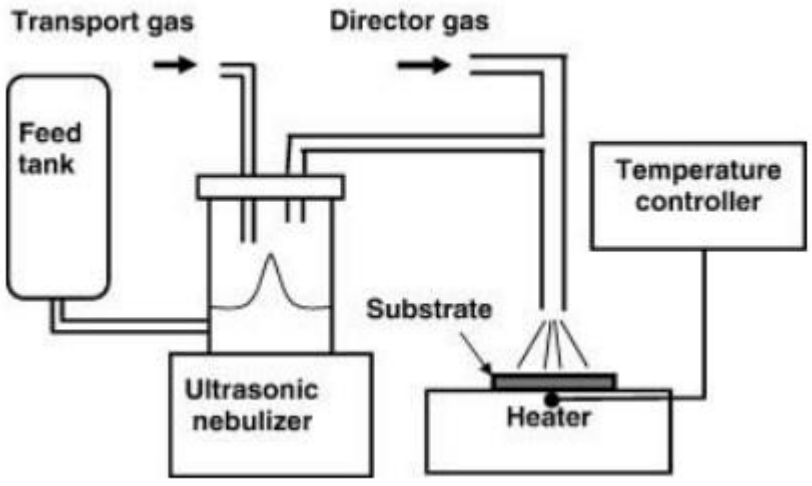

Fig. 8. Experimental setup of ultrasonic spray pyrolysis system [48]

1.3.3 Chemical bath deposition (CBD)

Chemical bath deposition (CBD) is a low-cost and facile chemical method for thin film deposition [26]. Substrate is immersed in the precursor solution, where chemical reactions between the reactants of the precursor solution lead to the formation of thin film onto the exposed substrate surface. Concentration of reactants, temperature of the solution and the pH solution determine the rate of deposition as well as thin film quality [25] [26].

Experimental setup for chemical bath deposition is given in Figure 9. Substrate is placed onto a substrate holder that is sunk into the vessel filled with the precursor solution. Vessel itself is placed in the chemical bath filled with water, which is then heated up to reach the desired solution temperature. Magnetic stirring avoids agglomeration of reacting particles in the solution. Besides temperature, solution is also made alkaline to slow down the rate of deposition. As to depositing CdS thin film, constituents, namely Cd^{2+} and S^{2-} ions, are brought in clustered with complexing agents to avoid immediate precipitation [25]. Ammonia is one of the complexing agents, which forms a cluster with the Cd^{2+} cation, but also increases the pH of the precursor solution, thus rendering the solution alkaline [25]. Alkaline solution is needed for the hydrolysis of thiourea that eventually gives away the S^{2-} anion [25]. Series of cluster mechanism reactions follow in which desired constituents swap clusters to eventually cause bulk precipitation. Hence, thin film condenses onto the substrate surface. This results from an equilibrium reaction, which implies the desired CdS compound formed by having less solubility, thus being thermodynamically favourable [25]. Therefore, apparently fast and simple deposition technique comprises of a sequence of reaction mechanisms that require accurate concentrations and close monitoring of the deposition conditions.

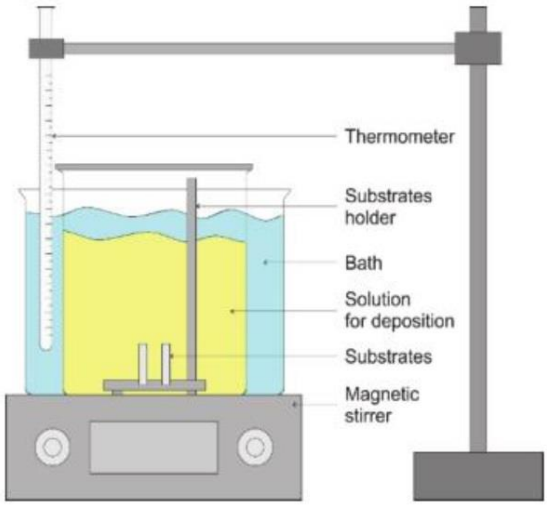

Fig. 9. Experimental setup for depositing thin films by chemical bath deposition [26]

1.4 Material characterisation techniques

1.4.1 Scanning electron microscopy (SEM)

Scanning electron microscopy (SEM) is used to study structural and topological properties of thin films, such as grain size, grain orientation and film thickness. The microscope is a probing system, where accelerated electrons are condensed and demagnified into a narrow beam that is focused on the specimen [53]. Incident beam electrons, which impinge on the specimen, can scatter back, cause emission of secondary electrons, or produce X-rays. Secondary electrons (SE) are collected to visualize the specimen surface and cross-section. Secondary electrons are produced, when incident electron dislodges an inner shell electron of the specimen atom. SE are low in energy, usually in the range of 2-5 eV, because they lose a large portion of energy to collisions [54]. For that reason, only SE generated at the proximity of surface can be collected, thus an image of surface will be produced. Image brightness depends upon the number of SE that were collected [54]. Image contrast results from the differing number of secondary electrons being collected at respective locations [55].

Schematic of a scanning electron microscope is shown in Figure 1 [56]. Electron gun emits electrons that are accelerated to 0.5-30 kV by negative anode bias [54]. When electrons pass through a lens system, condenser lenses converge the electrons into narrow beam that is then deflected by the magnetic coils and focused on the specimen by the objective lens. Electron beam diameter is about 5-10 nm and the magnitude of current is 10^{-12}-10^{-10} A [54]. When SEM carries out the raster scan, detected secondary electrons are detected on the Everhart-Thornley detector [54]. The signals are amplified and put together, thereby producing a visual image.

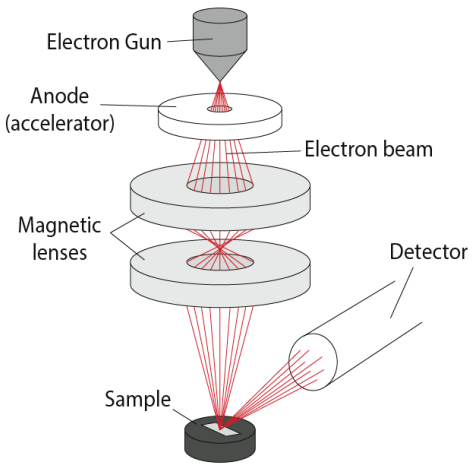

Figure 10. Schematic of scanning electron microscopy [56].

SEM is equipped with energy-dispersive X-ray spectroscopy (EDX) that is used to determine the chemical composition of the specimen [54]. As mentioned earlier, incident electron of the electron

beam can dislodge the inner shell electron of the specimen atom. In this case, the atom is left in an excited state. Excited atom can return to ground state provided that an outer shell electron relaxes onto the vacant site. This results in the emission of an X-ray photon with the energy that is the difference between the two energy levels. Emitted X-rays have characteristic wavelength that is specific to the specimen atom. Therefore, analysing the X-ray spectrum allows to determine the exact chemical composition of the specimen. [54] [57]

1.4.2 X-ray diffraction (XRD)

X-ray diffraction (XRD) is a characterisation technique for studying phase composition and crystal structure of specimen materials. X-rays have wavelength (10^{-10} m) that corresponds to the interatomic distances of a crystal lattice [58]. Ordered arrangement of atoms in a certain crystal direction establishes a crystal plane. These planes act as scattering centres to X-ray radiation [59]. When X-rays fall at an angle θ on the crystalline material, they pass through layers of atoms. Although diffraction occurs in all directions, diffraction maxima arise where X-rays reflect from the series of parallel crystal planes [58]. Figure 11 shows the schematic of Bragg-Brentano X-ray diffraction scan, where X-rays are detected along the symmetric direction [60]. This implies that both the incident X-rays and the diffracted X-rays make the same angle θ with respect to crystal plane [59]. X-rays are emitted by an X-ray tube and collimated by a slit [59]. Diffracted X-rays are detected by an ion chamber [59].

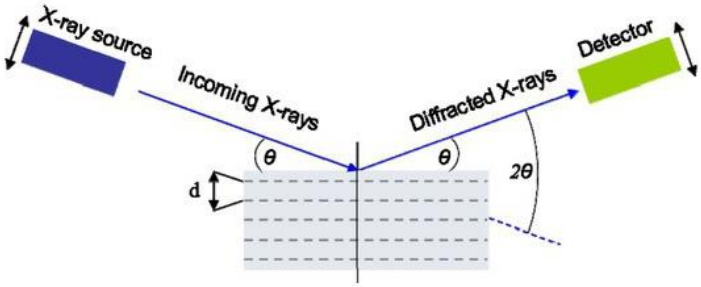

Fig. 11. Schematic of Bragg-Brentano X-ray diffraction, where incoming and diffracted X-rays both make the angle θ with respect to crystal plane [60]

Equation 2 represents Bragg law, which states that two X-rays, reflecting from two successive crystal planes, interfere constructively, when the phase difference is an integer number of wavelengths [58].

$$n\lambda = 2d \sin\theta \quad (2)$$

where n is an interger value, λ is the wavelength of the incident X-ray, θ is the angle incindent X-ray makes with respect to the specimen crystal plane [58].

Intensity of diffraction peaks depends upon the extent of constructive interference by the diffracting X-rays. More there are equally spaced and parallel crystal planes, higher the diffraction maximum [58] [59]. Obtaining diffraction maxima at a certain angle allows to find the crystallographic parameters of the specimen crystal.

1.4.3 UV-vis-NIR spectrophotometry

UV-vis-NIR spectrophotometry measures optical parameters of thin films. When a light wave impinges on the specimen material, it undergoes either transmission, absorption, or reflection. The absorptance of thin film can be determined through measuring transmittance and reflectance. When measuring transmittance and reflectance, light can scatter and thereby not reach the detector. Thus, the spectrophotometer is equipped with integrating sphere. The inner surface of the sphere is covered with highly reflective coating that enables the scattering light to be detected. Figure 12 shows the schematic of transmittance and transmittance measurements [25]. Transmittance of a thin film is measured with respect to bare glass substrate, where reflectance standard is a highly reflective barium sulfate [57].

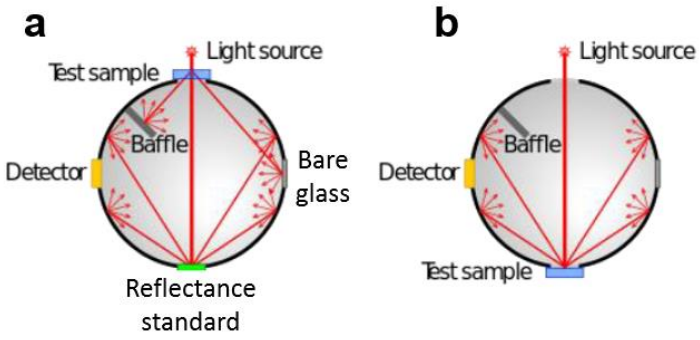

Fig. 12. Schematic of (a) transmittance and (b) transmittance measurement of thin film [25]

Absorption coefficient α can therefore be found by transforming Equation 3:

$$\frac{I}{I_0} = \frac{T}{1-R} = e^{-\alpha t} \tag{3}$$

where T is transmittance and R is reflectance, α is absorption coefficient in cm^{-1} and t is thin film thickness [25].

Optical band gap E_g can then be calculated by Equation 4:

$$(\alpha\hbar\omega)^n = A(\hbar\omega - E_g) \tag{4}$$

where A is constant, $\hbar$ is reduced Planck constant in eV·s, ω is the angular frequency of light photon in s^{-1}, E_g is the optical band gap in eV and n is an integer (1 for direct, 2 for indirect E_g) [25].

1.4.4 Van der Pauw measurement

Van der Pauw measurement determines the sheet resistance of the specimen material. Sheet resistance is a measure of resistance of a uniform sheet of film, defined as ohms per square [41]. Van der Pauw is a four-point probe technique, which is depicted in Figure 13. At the time of measurement, small current is passed through inner two probes , whilst voltage is measured between other two probes [44]. Subsequently, resistivity can be calculated using Equation 5:

$$\rho = R_{sq} \times d \tag{5}$$

where d is film thickness in cm, ρ is the film resistivity in Ω·cm, R_{sq} is the sheet resistance under illumination in Ω/sq [25] [44] [61].

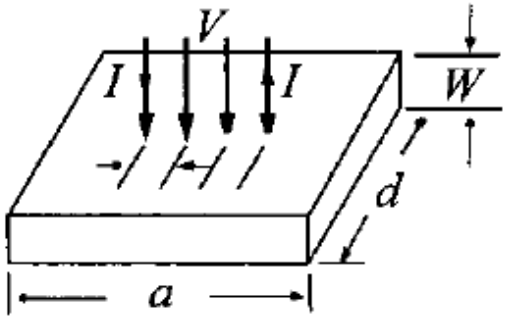

Fig. 13 Schematic of four-point probe configuration, where small current is passed through inner two probes, while outer two measure voltage. [44]

1.5 Solar cell characterisation techniques

1.5.1 Current-voltage (J-V) characteristics

Current-voltage (J-V) characteristic designates the quality of the solar cell. Solar cell behaves like a diode, which produces photocurrent under illumination. When a solar cell is illuminated and connected to an external load, it generates photovoltage [7]. Photocurrent flows across the p-n junction and self-biases the solar cell, reducing the electrostatic barrier and giving rise to diode current [7]. Diode current opposes the flow of photocurrent; therefore, it is called the reverse current. When applied bias is negative ($V_{bi} < 0$), diode current is negligible. Under positive bias ($V_{bi} > 0$), diode current undergoes exponential rise. Although diode current reduces the external photocurrent, rectifying diode-like behaviour is essential for charge separation and thereby solar cell operation.

For ideal diode model, external photocurrent can be found by Equation 6. The short-circuit current density (Jsc) is the photocurrent generated in the short circuit condition.

$$J(V) = J_0\left(e^{\frac{qV_{bi}}{k_BT}} - 1\right) - J_{SC} \quad (6)$$

where $J_0$is reverse saturation current, $k_B$is Boltzmann constant, q is elemental charge in C, T is temperature in K, V_{bi} is the applied bias in V and Jsc is the short circuit current density in mA cm^{-2} [7].

When the solar cell is illuminated, but it is not connected to external load, V_{bi} builds up until the diode current cancels out the generated photocurrent. This marks the maximum possible bias, which is the open circuit voltage (Voc). For ideal diode model, V_{OC} is given by Equation 7:

$$V_{OC} = \frac{kT}{q} ln\left(\frac{Jsc}{Jo} + 1\right) \quad (7)$$

where Jsc is the short circuit current density in mA cm^{-2}, $J_0$is the reverse saturation current, q is elemental charge in C, k is Boltzmann constant and T is temperature in degree Kelvin [7].

Fill factor (FF) characterises the "squareness" of the J-V characteristic [7], which can reveal the effect of series and shunt resistance. Series resistance reflects on the resistivity of materials and contacts impeding charge flow. High series resistance lowers the efficiency of charge collection. Shunt resistance alludes to the leakage current pathways within the cell. Larger is the shunt resistance, larger is the external photocurrent. [7] [45] Field factor is defined as the ratio, given by Equation 8:

$$FF = \frac{J_{mp}\, V_{mp}}{J_{SC}\, V_{OC}} \quad (8)$$

where J_{mp} is the maximum point for current density and V_{mp} is the is the maximum point for voltage, Jsc is the short circuit current density and Voc is the open circuit voltage [7].

Figure 14 shows a solar cell J-V characteristic measured in the dark and under illumination. In the dark condition, under forward bias there exists only diode current. Under illumination, there is external photocurrent that flows in the direction opposite to diode current, thus having negative value. Aforementioned J_{mp} and V_{mp} define the maximum power point of the solar cell characteristic. Therefore, power density of solar cells can be found by Equation 9:

$$P = J_{SC}\, V_{OC}\, FF = J_{mp}\, V_{mp} \quad (9)$$

where J_{mp} is the maximum point of current density in mA cm^{-2} and V_{mp} is the maximum point of voltage in V [7].

Photoconversion efficiency (PCE) is the paramount parameter that defines the ratio of maximum power density of solar cell to the solar irradiance and can thus be found by Equation 10:

$$PCE = \frac{J_{mp}\, V_{mp}}{P_S} \tag{10}$$

where J_{mp} is the maximum point of current density in mA cm^{-2} and V_{mp} is the maximum point of voltage in V and P_S is the solar irradiance in W m^{-2} [7].

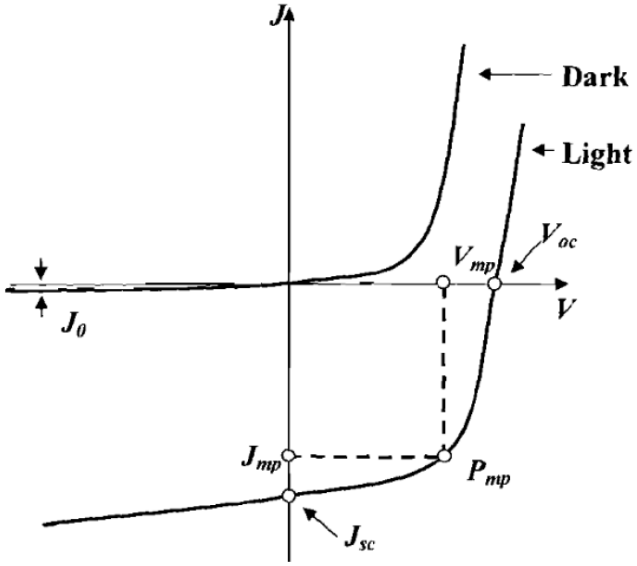

Fig. 14. J-V characteristic of a solar cell measured in the dark and under illumination [25].

1.5.2 External quantum efficiency (EQE)

External quantum efficiency (EQE) is defined as the ratio of the number of electron-hole pairs collected to the number of incident light photons. EQE is strongly dependent on the absorption coefficient of solar cell material, the efficiency of charge separation and the efficiency of charge collection [7]. Figure 15 compares an EQE of GaAs solar cell with solar photon flux density [7]. GaAs shows a very large EQE in the region between 500 and 900 nm, where there is also large solar photon flux density. Larger EQE infers that more light is being harvested. Therefore, EQE is an effective tool for evaluating solar cell performance.

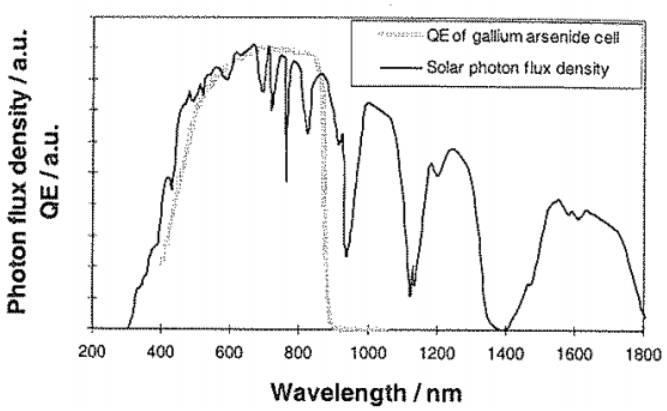

Fig. 15. EQE of GaAs cell together with the solar photon flux density. [7]

1.6 Summary of theoretical background and aims of the thesis

Based on the literature, the Sb_2Se_3 film properties and the Sb_2Se_3 solar cells can be summarised as follows:

1. Sb_2Se_3 is a promising photovoltaic absorber, as it exhibits high absorption coefficient and suitable optical band cap, which renders it a potential absorber layer in thin film solar cells. Sb_2Se_3 has intrinsic p-type conductivity like CdTe, owing to its antimony vacancies.
2. Single phase composition, high vapour pressure and low melting point make Sb_2Se_3 applicable to vapour transport deposition, close-spaced sublimation and rapid thermal evaporation deposition methods previously used for fabricating CdTe photovoltaic absorbers.
3. Sb_2Se_3 forms an orthorhombic crystal phase, where crystal phases of (211), (221) and (002) have been shown to enhance carrier transport. Crystal grains growing in the vertical direction lower the density of grain boundaries, which are the main cause for surface recombination in polycrystalline thin film solar cells.
4. CdS and TiO_2 films have been employed as window layers to Sb_2Se_3 absorber layer in the champion Sb_2Se_3 solar cells. Best CdS/Sb_2Se_3 solar cell employed CdS window that was deposited by chemical bath deposition. Record TiO_2/Sb_2Se_3 solar cell employed TiO_2 window layer that was deposited by spin-coating.

Knowing this led to aims of the following thesis:

1. To acquire knowledge of the working principles of thin film solar cells and the conventional deposition methods, post-deposition treatments, and characterisation techniques used for studying and analysing thin films and thin film solar cells.
2. To familiarise with the CSS method by fabricating Sb_2Se_3 thin films and solar cells
3. To describe the physicochemical processes responsible for the changes in the Sb_2Se_3 thin film properties induced by varying CSS deposition growth conditions.
4. To familiarise with CBD and USP deposition methods for growing CdS and TiO_2 window layers.
5. To devise a systematical study on the effect of substrate temperature in the close-spaced sublimation deposition process on the properties of Sb_2Se_3 thin films. To determine the optimal growth conditions for Sb_2Se_3 thin film solar cells.
6. To investigate the effect of different window layers on the Sb_2Se_3 film properties and the Sb_2Se_3 solar cells.

2. EXPERIMENTAL

Figure 16 depicts the three fabricated CSS-CdS/Sb_2Se_3, TiO_2/Sb_2Se_3 and CBD-CdS/Sb_2Se_3 solar cells. While studying the effect of substrate temperature on the Sb_2Se_3 film properties and the Sb_2Se_3 solar cell, I employed only the (1) CSS-CdS/Sb_2Se_3 configuration, as shown in Fig. 15a. Sb_2Se_3 film was deposited at different substrate temperatures of 300 to 450 °C. CdS window layer was deposited by CSS. All Sb_2Se_3 films were characterised by SEM, EDX, and XRD. Optimal Sb_2Se_3 film underwent UV-vis-NIR and van der Pauw measurements. Sb_2Se_3 PV devices were characterised by J-V characteristic and EQE.

While studying the effect of different window layers on the Sb_2Se_3 film properties and the Sb_2Se_3 solar cell, I employed two other – (2) TiO_2 and (3) CBD-CdS – window layers, as shown in Fig15b,c, respectively. TiO_2 was deposited by USP, CBD-CdS was deposited by CBD. Sb_2Se_3 film was always deposited at the optimal substrate temperature that had been previously determined. All three window layers were characterised via UV-vis-NIR, van der Pauw and XRD measurements. Sb_2Se_3 films were characterised by SEM and XRD. CSS-CdS/Sb_2Se_3, TiO_2/Sb_2Se_3 and CBD-CdS/Sb_2Se_3 PV devices were characterised by J-V characteristic and EQE.

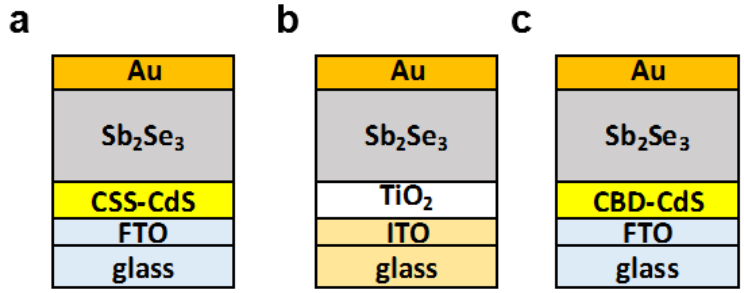

Fig. 16. Schematic of (a) CSS-CdS/Sb_2Se_3, (b) TiO_2/Sb_2Se_3 and (c) CBD-CdS/Sb_2Se_3 solar cells

2.1 Fabricating CdS/Sb_2Se_3 solar cells

Glass/FTO substrate preparation

Soda-lime glass substrates coated with fluorine-doped tin oxide (FTO) for CdS film deposition. FTO film thickness is ~200 nm with sheet resistance of ~25 Ω/sq. Preparation of the glass/FTO substrates included cutting substrates into 20 x 20 mm area, leaving substrates in a 10 g $K_2Cr_2O_7$ + 10 mL H_20 + 100 mL H_2SO_4 solution for 2-3 h at room temperature, then rinsing substrates with deionised water and finally drying in air.

2.1.1 Fabricating CSS-CdS/Sb_2Se_3 solar cells

CSS-CdS deposition by close-spaced sublimation (CSS)

CdS thin films were deposited onto glass/FTO substrates by CSS. The source CdS in solid powder form (99% wt), purchased from Sigma-Aldrich. Source temperature was heated to 650 °C and substrate temperature was heated to 350 °C. Source temperature and substrate temperature were held constant throughout CSS-CdS film deposition: Deposition time was 35 s.

Sb_2Se_3 deposition by CSS onto CSS-CdS substrate

Sb_2Se_3 absorber layers were deposited by CSS onto glass/FTO/CSS-CdS substrates. The source material was Sb_2Se_3 in solid powder form (99% wt), purchased from Sigma-Aldrich. Source temperature was heated to 520 °C. Substrate temperature was heated to different temperatures in the range between 300 and 450 °C .Deposition time was 45 s.

2.1.2 Fabricating CBD-CdS/Sb_2Se_3 solar cells

CBD-CdS deposition by chemical bath deposition (CBD)

I used a precursor solution consisting of $CdSO_4$, NH_4SO_4, NH_4OH, NH_4Cl and deionized water, previously made for previous studies [25] [26]. Glass/FTO substrates were placed onto a holder and put into the solution in a quartz bath. Solution was then heated to 85 °C. At 85 °C, thiourea was added, which initiated the chemical reaction sequence. Solution was stirred throughout the time of the reactions. Deposition time was set to 10 min, after which substrates were ultrasonicated in deionised water for 5 min at 50°C. Finally, substrates were dried with a fan.

Sb_2Se_3 deposition by close-spaced sublimation (CSS) onto CBD-CdS substrate

Sb_2Se_3 absorber layers were deposited by CSS onto glass/FTO/CBD-CdS substrates. Source temperature was heated to 520 °C. Substrate temperature was heated to 450 °C .Deposition time was 45 s.

Au back contact deposition

Au back contacts were vacuum-evaporated onto *CSS-CdS/*Sb_2Se_3 and *CBD-CdS/*Sb_2Se_3 films. Area of back contact was 25 mm^2. Later, a thin layer of In was soldered onto the Au contact to prevent the surface from being damaged by scratching of electrical contacts.

2.2 Fabricating TiO_2/Sb_2Se_3 solar cell

Glass/ITO substrate preparation

Soda-lime glass substrates coated with indium-doped tin oxide (ITO) were used for TiO_2 film deposition. Film thickness of ITO is ∼150 nm with sheet resistance of ∼25 Ω/sq. Preparation of the glass/ITO substrates including cutting substrates into size of 20 x 20 mm area, rinsing with ethanol, ultrasonicating substrates in ethanol bath for 10 min, and finally drying with compressed air.

TiO_2 deposition by ultrasonic spray pyrolysis (USP)

TiO_2 films were deposited by USP onto glass/ITO substrates. The substrate was heated to 340 °C. I used precursor solution of TTIP and AcAc with molar ratio of 1:4 dissolved in ethanol. Concentration of TTIP was 0.1 M. The deposition time was 15 min. Compressed air with 5 L/min was used as carrier gas. After deposition, TiO_2 films underwent annealing at 450 °C for 30 min in air.

Sb_2Se_3 deposition by close-spaced sublimation

Sb_2Se_3 absorber layers were deposited by CSS onto glass/ITO/TiO_2 substrates. Source temperature was heated to 520 °C. Substrate temperature was heated to 450 °C .Deposition time was 45 s.

Au back contact deposition

Au back contacts were vacuum-evaporated onto *CSS-CdS/*Sb_2Se_3 and *CBD-CdS/*Sb_2Se_3 films. Area of back contact was 25 mm^2. Later, a thin layer of In was soldered onto the Au contact to prevent the surface from being damaged by scratching of electrical contacts.

2.3 Material characterisation

Crystal growth and structure of were visualised by Zeiss EVO-MA15 scanning electron microscope (SEM) equipped with a Zeiss HR FESEM Ultra 55 system. Top-view and cross-sectional images of Sb_2Se_3 films were made by Dr. Olga Volobujeva from the Department of Materials and Environmental Technology at Tallinn University of Technology.

I carried out the XRD measurements of window layers and Sb_2Se_3 films with a Rigaku Ultima IV diffractometer by Cu Kα radiation (λ = 1. 54 Å, 40 kV, 40 mA). XRD patterns were analysed with Rigaku PDXL software. Crystal phases were obtained by using data issued by the Joint Committee on Powder Diffraction Standards (JCPDS). The data files used were as follows:

- Sb_2Se_3 – JCPDS 01-089-0821
- CSS-CdS – JCPDS 00-041-1049
- TiO_2 – JCPDS 98-015-4604
- CBD-CdS – JCPDS 01-089-0440

I measured transmittance and reflectance spectra of window layers and Sb_2Se_3 films by Jasco V-670 UV-Vis spectrophotometer equipped with an integrating sphere. Spectra were acquired in the wavelength region between 250 and 1500 nm. Optical band gaps were calculated using the Equations 3 and 4, as shown in Section 1.3.3.

I measured sheet resistance of window layers and Sb_2Se_3 films by van der Pauw four-point probe technique. Resistivities were calculated using the Equation 5, as shown in Section 1.4.4. Film thickness was measured by SEM.

2.4 Device characterisation

I measured J-V characteristic of CSS-CdS/Sb_2Se_3, TiO_2/Sb_2Se_3 and CBD-CdS/Sb_2Se_3solar cells using an AUTOLAB PGSTAT 30 and an Oriel class A solar simulator 91159A (100 mW cm^{-2}, AM1.5) at the Laboratory of Thin Film Chemical Technologies at Tallinn University of Technology.

I measured EQE of CSS-CdS/Sb_2Se_3, TiO_2/Sb_2Se_3 and CBD-CdS/Sb_2Se_3solar cells using a 300 W xenon lamp and a SPM-2 Carl Zeiss-Jena monochromator that worked at 30 Hz.

3. RESULTS AND DISCUSSION

3.1 Effect of substrate temperature on the Sb_2Se_3 film properties and the Sb_2Se_3 solar cell performance

Section 3.1 reports on the effect of substrate temperature on the Sb_2Se_3 film properties and the Sb_2Se_3 solar cell performance. Herein, Sb_2Se_3 films were deposited by close-spaced sublimation at different substrate temperatures of 300 to 450°C. In this section, CdS window layer was deposited by close-spaced sublimation (CSS-CdS), thus CSS-CdS/Sb_2Se_3 was made, as shown in Fig. 16a.

3.1.1 Effect of substrate temperature on the Sb_2Se_3 film properties

Sb_2Se_3 films were first deposited by CSS onto the glass/FTO/CSS-CdS substrates. Experimental is further explained in Section 2.1.1. Source temperature was heated to 520 °C. Substrate temperature was varied between 300 and 450 °C. The respective temperature range was chosen with regard to previous studies [11] [12] [17] [18].

SEM study revealed a strong dependence of the crystal growth of the deposited Sb_2Se_3 films upon the substrate temperature at the Sb_2Se_3 film deposition. Figure 17 shows top-view and cross-sectional images of glass/FTO/CdS/Sb_2Se_3 structures with Sb_2Se_3 films deposited at substrate temperatures of 300 to 450 °C. The Sb_2Se_3 films deposited at 300 °C (Sb_2Se_3-300 °C) exhibit plate-shaped grains with sharp ends, as seen in Fig. 17a. Grains look ribbon-like, elongated and thin, and have grown either upright, curved or tilted on the substrate surface, as seen in Fig. 17e. Structure density is very low, because thin ribbons leave a lot of channels and voids between them. Film thickness is ∼7 μm. Increasing substrate temperature to 350°C (Sb_2Se_3-350 °C) produces similar plate-like grain ends, as seen in Fig. 17b, yet the grains are larger in width, showing more columnar-like grains, as seen in Fig. 17f. Interestingly, all grains are tilted at the same angle. Although grains grew in size, structure still incorporates high density of voids and channels. Film thickness of Sb_2Se_3-350 °C is ∼12 μm. At substrate temperature of 400°C (Sb_2Se_3-400 °C), grains have irregular shapes, but show round corners, as seen in Fig. 17c. Film is denser, especially at the proximity of substrate surface, evidenced by lower density of voids, as seen in Fig. 17g. Crystal orientation and size distribution is random. Film thickness is smaller at ∼9 μm. Substrate temperature increase to 450°C (Sb_2Se_3-450 °C) produces the densest structure, as seen in Fig. 17d. Grains are again irregularly shaped with round corners, but they are most closely-packed. High packing density also results in the lowest density of voids, as seen in Fig. 17h. Cross-sectional view indicates the grains show various sizes but are larger than in Sb_2Se_3-400 °C. Of the four structures, Sb_2Se_3-450 °C exhibits clearly the most compact film structure. Film thickness is ∼7 μm. EDX measurements confirmed the

presence of Sb_2Se_3 films with the corresponding stoichiometric ratio of 2:3 for respective Sb:Se atoms.

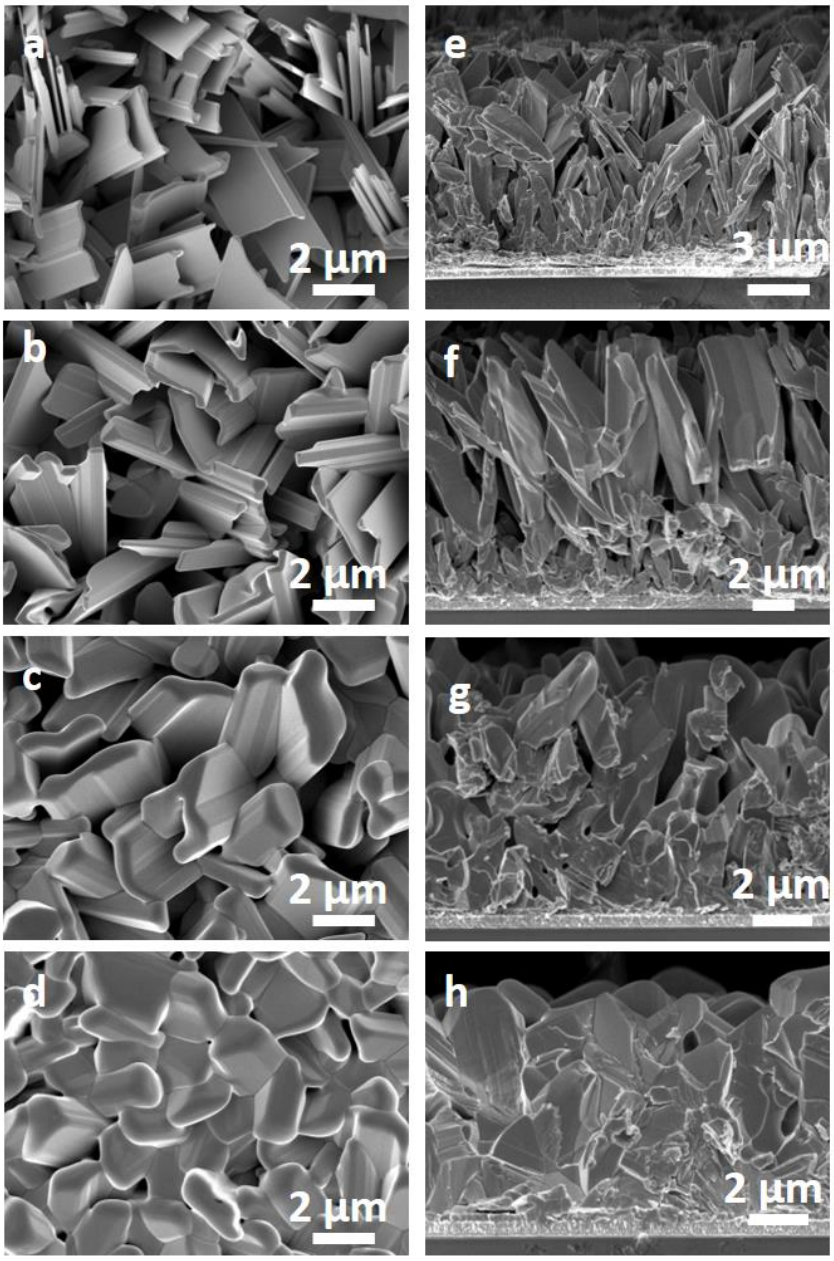

Fig. 17. Morphology of Sb_2Se_3 films deposited at substrate temperatures of 300 to 450 °C. Top-view (a-d) SEM images of Sb_2Se_3 with different substrate temperatures, (a) 300 °C (b) 350 °C (c) 400 °C and (d) 450 °C. Cross-sectional SEM mages of Sb_2Se_3 with different substrate temperatures, (e) 300 °C (f) 350 °C (g) 400 °C and (h) 450 °C

Figure 18 displays the XRD patterns of Sb_2Se_3 films deposited at different substrate temperatures of 300 to 450 °C. Sb_2Se_3 diffraction peaks were analysed with respect to PDF JCPDS 01-089-0821. Peaks at 28.2°, 31.1°, 32.2°, 45.1° and 45.6°, present in all four Sb_2Se_3 films, refer to (211), (221), (301), (151), (002) crystal phases, which are characteristic to orthorhombic Sb_2Se_3 crystal structure. Sb_2Se_3-300 °C has grains that are (211)-, (221)- and (002)-orientated, as was shown in Fig. 17e.

Crystal grains do grow in the vertical direction. Sb_2Se_3-350 °C has main crystal phases of (211), (221) and increased (002) phase, which is evidenced by crystal grains growing upright, as seen in Fig. 17f. Sb_2Se_3-400 °C reveals main preference for (221), (221) and (301) crystal phase. The emergence of (301) crystal phase can be explained through greater crystal growth in the lateral directions, as was seen in Fig. 17g. and reduced peak intensity for (002) crystal phase, compared with Sb_2Se_3-350 °C. Sb_2Se_3-450 °C has preference for crystal phases (221), (301) and (151), which refer to tilted crystal grains.

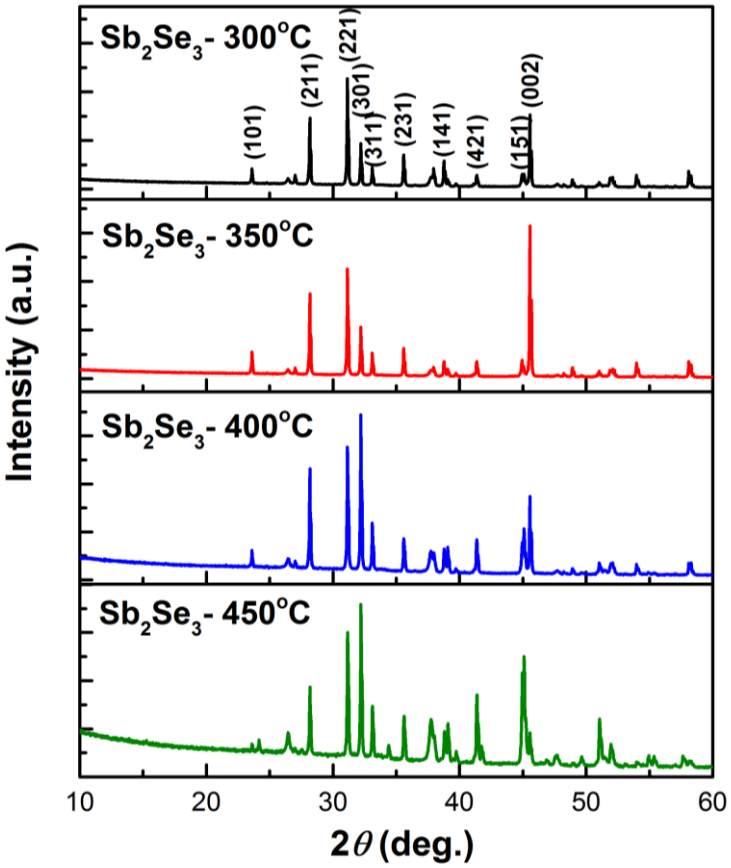

Fig. 18. XRD patterns of Sb_2Se_3 films deposited at substrate temperatures of 300 to 450°C

Substrate temperature affects the nucleation density, adatom mobility, surface diffusion and coalescence rate that together drive the crystal growth [62]. In close-spaced sublimation, vapour particles condense onto the substrate, where they undergo transition into solid phase. The first set of particles, called adatoms, form nucleation centres to which subsequent molecules can bind. Depending on the substrate temperature, adatoms can form new nuclei, diffuse across surface and bind to other adatoms, bind to step or kink sites, or re-evaporate [62]. Re-evaporation is not desired, thus adatoms should be held on the surface. It transpires that the stability of adatoms and therefore nucleation density can be explained through the thermodynamic theory of nucleation [10]. This theory states that after a series of collisions, adatoms must form a nucleus that has a

radius greater than the critical radius. Only then does the nucleus avoid re-evaporation. Critical radius is associated with the substrate temperature and the vapour pressure [62]. Higher is the substrate temperature, higher is the limit of the critical radius. This implies that at higher substrate temperatures, adatoms are more prone to re-evaporation, because the probability of forming a stable nucleus is smaller [62]. Hence, at higher temperatures, the nucleation density is low, which means there are fewer nucleation centres on the substrate surface.

The nuclei that attain critical radius can grow larger by the addition of material from vapour or diffusing adatoms [62]. They start forming islands, which at one point can overlap and lead to coalescence into a single crystal grain. This is energetically favourable, because it lowers the total surface energy of the two islands. Yet coalescence is also dependent on the substrate temperature. The rate of coalescence relies on the rate of material transfer between the two islands [62]. If the substrate temperature is low, low is the diffusion rate and mobility of adatoms. Therefore, grains grow larger at higher substrate temperatures, because the conditions allow for faster material transfer. Diffusion rate and adatom mobility also explain the channel or void formation within the crystal structure. The coalescence of neighbouring islands is usually incomplete, thus leaving channels between them [62]. Nevertheless, these channels can be filled by secondary nucleation, which can eventually help form a dense void-free thin film. At high temperature, these new nuclei have enough mobility to add to the larger crystal grains. At low temperature, the diffusion rate is too low for secondary nuclei to coalesce with larger islands.

These concepts can be used to explain the crystal growth of the Sb_2Se_3 films at different substrate temperatures. In case of Sb_2Se_3-300 °C, low substrate temperature produced large nucleation density. Because of low diffusion rate and adatom mobility, the single island growth rate was greater than that of coalescence between neighbouring islands. For this reason, Sb_2Se_3-300 °C exhibited large number of elongated grains with wide channels between them, as seen in Fig. 17e. Sb_2Se_3-350 °C also showed high nucleation density. Higher substrate temperature yielded wider grains, yet the structure still incorporated large number of channels and voids, as seen in Fig. 17f. Sb_2Se_3-400 °C was the first structure to show grains with round corners, which refer to reduced surface energy [62], as seen in Fig. 17c. Grains are larger and have more uniform size distribution, which can be attributed to lower nucleation density and higher adatom mobility, which enabled for greater coalescence. Consequently, grains produce a more compact film with less voids. Nevertheless, the structure still seems to incorporate high density of grain boundaries. Sb_2Se_3-450 °C had the most compact structure with largest grains, which resulted from lower nucleation density and higher adatom mobility. High temperature allowed the formation of less nuclei, which

eventually got larger due to higher coalescence rate. This also resulted in the reduced density of grain boundaries. It appears the coalescence occurred more in the lateral direction, as the Sb_2Se_3-400 °C and Sb_2Se_3-450 °C films have suppressed (002) crystal phase and have had the emergence of (301) crystal phase, as seen in Fig. 18.

3.1.2 Effect of substrate temperature on the Sb_2Se_3 solar cell performance

Figure 19 shows the current-voltage characteristics (J-V) of glass/FTO/CdS/Sb_2Se_3/Au solar cells with Sb_2Se_3 films deposited at substrate temperatures of 300 to 450 °C. Main photovoltaic parameters are listed in Table 1.

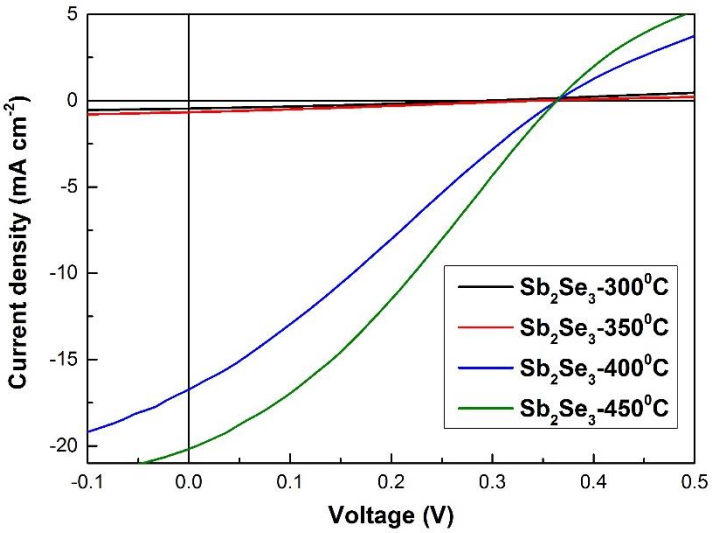

Fig. 19. Current-voltage (J-V) characteristics of glass/FTO/CdS/Sb_2Se_3/Au solar cells with Sb_2Se_3 deposited at substrate temperatures of 300 to 450 °C

Solar cells show strong dependence upon the substrate temperature at which Sb_2Se_3 films were deposited. This is evidenced by the fact that Sb_2Se_3-300 °C and Sb_2Se_3-350 °C solar cells barely functioned, whereas Sb_2Se_3-400 °C and Sb_2Se_3-450 °C solar cells produced photocurrent, as seen in Fig. 19. Sb_2Se_3-300 °C and Sb_2Se_3-350 °C solar cells achieve comparable V_{OC} and FF values with Sb_2Se_3-400 °C and Sb_2Se_3-450 °C, but produce negligible current, as seen in Table 1. Negligible current can be attributed to the low quality of the Sb_2Se_3 absorber, incorporating high density of channels that increase shunting pathways across the junction. Although Sb_2Se_3 was stated to possess benign grain boundaries [17], herein the high density of grain boundaries, as seen in Fig. 17 e and f, is still likely to contribute to the surface recombination. Lower V_{OC} value of 0.29 V for Sb_2Se_3-300 °C solar cell alludes to low-quality formation of the depletion region, which can be explained through voids between nucleation sites on the substrate surface. As for Sb_2Se_3-350 °C, V_{OC} of 0.34 V can be attributed to more compact crystal growth at the proximity of the substrate surface, which

consolidated junction formation. Sb_2Se_3-400 °C produces V_{OC} of 0.36 V, which suggests the increase of substrate temperature had minimal effect on improving the depletion region. This value is comparable to the V_{OC} of 0.42 V recorded for the champion CdS/Sb_2Se_3 solar cell. However, the J_{SC} of 16.5 mA cm^{-2} marks a drastic increase compared to Sb_2Se_3-300 °C and Sb_2Se_3-350 °C solar cells. The generation of photocurrent is probably the result of Sb_2Se_3-400 °C film having a distinct crystal structure. Sb_2Se_3-400 °C gave a compact film with larger grains and less voids, reducing the density of grain boundaries and thus enabling carriers to diffuse into the depletion region. Interestingly, Sb_2Se_3-400 °C shows no improvement of the FF value, as seen in Table 1, which suggests the resistance to carriers in the structure is of similar magnitude as in Sb_2Se_3-300 °C and Sb_2Se_3-350 °C solar cells. Therefore, it signifies the importance of having uniform coverage of the Sb_2Se_3 at the interface for efficient charge separation. The Sb_2Se_3-400 °C is denser at the proximity of the depletion region, as shown in Fig. 17g, than in Sb_2Se_3-300 °C and Sb_2Se_3-350 °C films, as shown in Fig. 17e and f, respectively. Overall, Sb_2Se_3-400 °C solar cell achieved PCE of 1.6%. Most importantly, Sb_2Se_3-450 °C solar cell produced highest J_{SC} of 16.5 mA cm^{-2} and highest FF of 31.7%, thus attaining also the highest PCE of 2.3%. Best performance can be attributed to the highest quality of Sb_2Se_3-450 °C film, which had the densest structure with largest grains, least voids and lowest density of grain boundaries, as shown in Fig. 17h. Larger grains and lower density of grain boundaries explain both the increase in J_{SC} and V_{OC}, because they reduce the probability of carriers bumping into surface defect states at grain boundaries. This in turn reduces the probability of recombination. Although, J_{SC} of 20.0 mA cm^{-2} is considered the best in this context, CdS/Sb_2Se_3 solar cell has been shown to produce J_{SC} values of 29.9 mA cm^{-2} [12]. Also, FF of 31.7 of Sb_2Se_3-450 °C solar cells is significantly lower than the FF of 60.4%, achieved by the record CdS/Sb_2Se_3 solar cell [12]. Hence, the CdS/Sb_2Se_3 solar cell can still be substantially improved. It is important to note that the record Sb_2Se_3 photovoltaic devices have been attained with a Sb_2Se_3 crystal structure where grains span the whole layer [11] [12] [17] [18]. This minimises the effect of surface recombination, because the minority carriers can travel across the grain without being trapped at the surface defect states [13]. It must also be noted that the crystal phase of (002), which was predominantly seen in Sb_2Se_3-300 °C and Sb_2Se_3-350 °C films, as shown in Fig. 18, did not provide better carrier transport. This proves the fact that efficient light harvesting in a superstrate configuration rather requires dense structure with large adjoined grains. It must also be noted that low FF for all four solar cells may refer to the high resistivity of the Sb_2Se_3 film and the CdS window layer. Van der Pauw measurement in the dark revealed the electrical resistivity of both the Sb_2Se_3-450 °C absorber and the CSS-CdS window is $>10^6$ Ω·cm, which is highly detrimental to efficient carrier transport. This suggests lower electric field across the depletion region and higher resistance to minority carriers travelling within the absorber material. Carrier density, which is inversely related to electrical resistivity, has been shown

to be low for Sb_2Se_3 absorber. Chen et al. found that the carrier concentration of the as-deposited Sb_2Se_3 film was 10^{13} cm^{-3}, while the optimal carrier density for photovoltaic absorbers is at $\sim 10^{16}$ cm^{-3} [10] [19].

Table 1. Photovoltaic parameters of glass/FTO/CdS/Sb_2Se_3/Au solar cells with Sb_2Se_3 films deposited at substrate temperatures of 300 to 450°C

T_{sub} (°C)	V_{OC} (V)	J_{SC} (mA cm^{-2})	FF (%)	PCE (%)
300	0.29	0.5	30.1	0.0
350	0.34	0.6	27.3	0.1
400	0.36	16.5	27.1	1.6
450	0.36	20.0	31.7	2.3

External quantum efficiency (EQE) and normalised EQE of glass/FTO/CdS/Sb_2Se_3/Au solar cells with Sb_2Se_3 deposited at substrate temperatures of 400 and 450 °C are given in Fig. 20. The graph only includes Sb_2Se_3-400 °C and Sb_2Se_3-450 °C solar cells, because the respective devices enabled for considerable photoconversion. The two curves reveal that the Sb_2Se_3-400 °C and Sb_2Se_3-450 °C solar cells have largest EQE at ~700 nm. As for Sb_2Se_3-400 °C solar cell, EQE maximum is close to 70%. At the same time, Sb_2Se_3-450 °C solar cell reaches EQE of 93%, which is very high for a photovoltaic device [7]. In the wavelength region between 340 and 900 nm., Sb_2Se_3-450 °C solar cell has larger EQE that explains its superior performance. This can again be attributed to the superior Sb_2Se_3-450 °C film quality, where denser structure with larger grains improves the charge transport and separation. Normalised EQE shows the charge collection at different wavelengths is nearly the same in the two solar cells. EQE has steep declines at both shorter and longer wavelengths. Parasitic absorption at lower wavelengths is related to the light absorption by the CdS window layer [13]. Despite this, EQE of Sb_2Se_3-450 °C is still larger below ~500 nm, which marks the absorption edge of the CdS window (E_g = 2.5 eV) [25]. This suggests that certain amount of collected minority carriers could have been generated within the window layer. Low EQE at longer wavelengths is related to back surface recombination and low minority carrier diffusion lengths. Chen et al. [19] reported that (221)-orientated Sb_2Se_3 grains have diffusion length in the range of 0.3-0.6 µm, which is at least ten times smaller than the film thickness of Sb_2Se_3-400 °C and Sb_2Se_3- 450 °C films. Comparing Sb_2Se_3-400 °C and Sb_2Se_3-450 °C solar cells with previous studies, EQE at longer wavelengths, especially in the region between 500 and 900 nm, explains the inferior performance to record CdS/Sb_2Se_3 photovoltaic devices [12] [17].

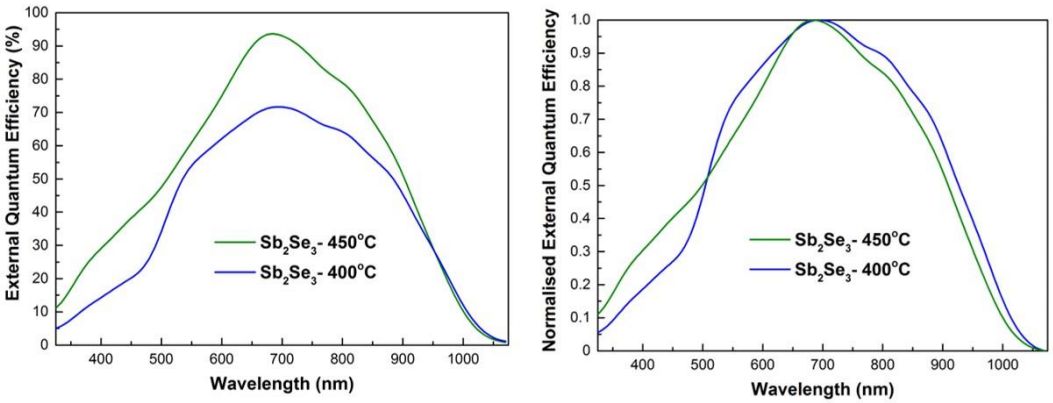

Fig. 20. EQE and normalised EQE of glass/FTO/CdS/Sb_2Se_3/Au solar cells with Sb_2Se_3 films deposited at substrate temperatures of 400 °C and 450 °C

In sum of Section 3.1, a systematic study was carried out to investigate the effect of substrate temperature on the Sb_2Se_3 film properties and the Sb_2Se_3 solar cell performance. The Sb_2Se_3 films were deposited by CSS at different substrate temperatures in the range between 300 and 450 °C. Herein, the Sb_2Se_3 films were grown onto glass/FTO/CdS substrates, in which CdS was deposited by CSS (CSS CdS). Results showed that there was strong correlation between the substrate temperature applied at the CSS deposition and the following properties of the grown Sb_2Se_3 films. Increasing substrate temperature improved the density of the crystal structure, increased crystal grains, reduced the density of grain boundaries and the density of voids. This was explained through the physicochemical processes involved in the CSS deposition process. Solar cells employing Sb_2Se_3-300 °C and Sb_2Se_3-350 °C did not function, but solar cells employing Sb_2Se_3-400 °C and Sb_2Se_3-450 °C achieved PCE of 1.6% and 2.3%, respectively. Highest performance at 450 °C was attributed to the highest quality of the Sb_2Se_3 absorber, which through reduction of grain boundaries and increased crystal grains and structure density facilitated carrier transport. In conclusion, applying substrate temperature of 450 °C proved optimal for photovoltaic performance.

3.2 Effect of window layer on Sb_2Se_3 film properties and Sb_2Se_3 solar cell performance

Section 3.2 reports on the investigation into the effect of different window layers on the Sb_2Se_3 film properties and the Sb_2Se_3 solar cell performance. Herein, Sb_2Se_3 absorber film was always deposited at the optimal substrate temperature of 450 °C, as determined in Section 3.1.

Altogether, there were three different window layers partnering Sb_2Se_3 absorber: (1) CdS window layer deposited by CSS (CSS CdS), (2) TiO_2 window layer deposited by ultrasonic spray pyrolysis and (3) CdS window layer deposited by CBD (CBD CdS), as shown in Fig. 16a, b and c, respectively.

Before analyses of the Sb_2Se_3 films and the Sb_2Se_3 solar cells, there is an overview of the optoelectronic properties of window layers and absorber, and morphological properties of the window layers.

3.2.1 Optoelectronic properties of CSS CdS, TiO_2, CBD CdS and Sb_2Se_3

Electrical resistivity

Sheet resistance, thickness and resistivity values of all three window layers and the absorber layer are listed in Table 2. To calculate resistivity, the sheet resistance measured in the dark was multiplied with the respective thickness of the film measured by SEM. In striking contrast with CSS CdS and TiO_2, CBD CdS window layer exhibits substantially lower resistivity of 100 Ω·cm. Lower resistivity can be attributed to higher carrier concentration of $>10^{14}$ cm^{-3} [63] compared to other two window layers. As for CSS CdS, sheet resistance was too large to be measured both in dark and light condition, which explains the need for post-deposition treatment, usually in the form of $CdCl_2$ chemical treatment that would increase the carrier concentration [12] [16] . Compared to CBD CdS, TiO_2 window layer resistivity is three orders of magnitude larger at 2×10^5 Ω·cm. Sb_2Se_3 also records very high series resistance and ultimately highest resistivity due to much larger film thickness. Reduction in sheet resistance of TiO_2 and Sb_2Se_3 layers was seen under light, which can be related to complementary carrier generation, thereby saturating more defect states and lowering resistivity [7].

Table 2. Sheet resistance (in dark, R_D, and under light ,R_L), thickness and resistivity values of CSS CdS, TiO_2, CBD CdS window layers and Sb_2Se_3 absorber layer

Layer	R_D (Ω/sq)	R_L (Ω/sq)	Thickness (nm)	ρ_D (Ω cm)
CSS CdS	$>5\times10^{10}$	$>5\times10^{10}$	100	$>5\times10^5$
TiO_2	3×10^{10}	10^{10}	200	6×10^5
CBD CdS	10^7	10^6-10^7	100	100
Sb_2Se_3	10^{10}	10^9	7000	7×10^6

Optical band gap E_g

Figure 21 displays Tauc plots and calculated band gap E_g values for all three window layers and the Sb_2Se_3 absorber layer. E_g values of CSS CdS, TiO_2 and CBD CdS windws were 2.5 eV, 3.4 eV and 2.5 eV, as shown in Fig. 21a, b and c, respectively. Despite applying different deposition techniques, both CdS windows share the same band gap value, which complies with previous studies [18] [25]. Significantly larger band gap of TiO_2 is slightly higher than the usually reported values [30], but this can be attributed to large density of oxygen vacancies incorporated in the titania structure [43] [64]. The Sb_2Se_3 absorber E_g was ~1.2 eV, as shown in Fig. 21d, which complies with previous studies [17] [19] [22].

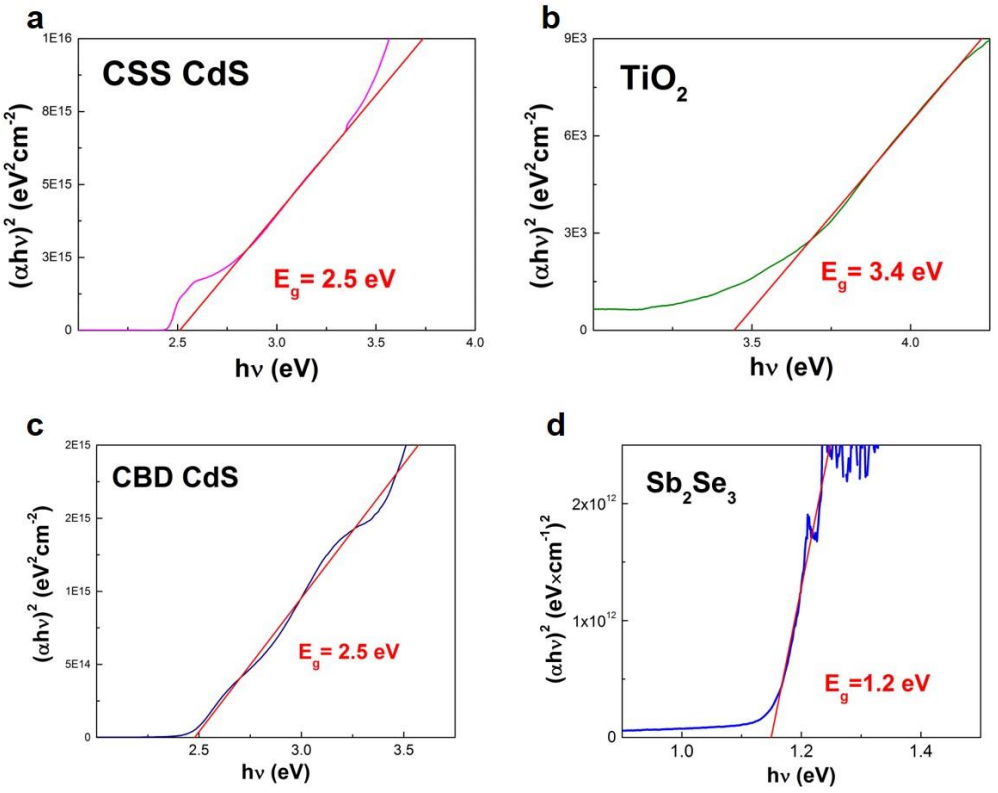

Figure 21. Tauc plot and optical band gap of (a) CSS CdS, (b) TiO_2 , (c) CBD CdS and (d) Sb_2Se_3 layer

3.2.2 Structural properties of CSS CdS, TiO_2 and CBD CdS window layers

Figure 22 displays XRD patterns of all three window layers. CSS CdS XRD pattern, as shown in Fig. 22a, reveals peaks at 26.7°, 48.0° and 51.7°, which refer to respective crystal phases of (002), (103) and (112) that are characteristic of hexagonal wurtzite crystal structure [25]. Remainder of peaks refer to the FTO/glass substrate [65]. TiO_2 XRD pattern, as shown in Fig. 22b, exhibits peaks at 25.3°, 37.5° and 48.1°, which correspond to (101), (004) and (200) crystal phases of tetragonal anatase structure [66]. Rest of the peaks refer to the glass/ITO substrate [67]. CBD CdS XRD pattern, as shown in Fig. 22c, reveals peaks at 26.9° and 51.7°, which correspond to respective crystal phases (111) and (311) of cubic zinc blende structure [25]. Remainder of peaks refer to glass/FTO substrate [65]. Therefore, CSS CdS and CBD CdS window layers possess different crystal structures, which may explain the huge difference in the electrical resistivity, as seen in Table 2. Although, TiO_2 window layer does exhibit crystal grains of anatase phase, the structure is known to be predominantly amorphous [46]. It is observed that post-deposition annealing does introduce anatase crystal phase, which improves film conductivity, yet amorphous phase of titania is still desired in solar cells due to its high density of oxygen vacancies that gives TiO_2 its n-type conductivity [30] [43].

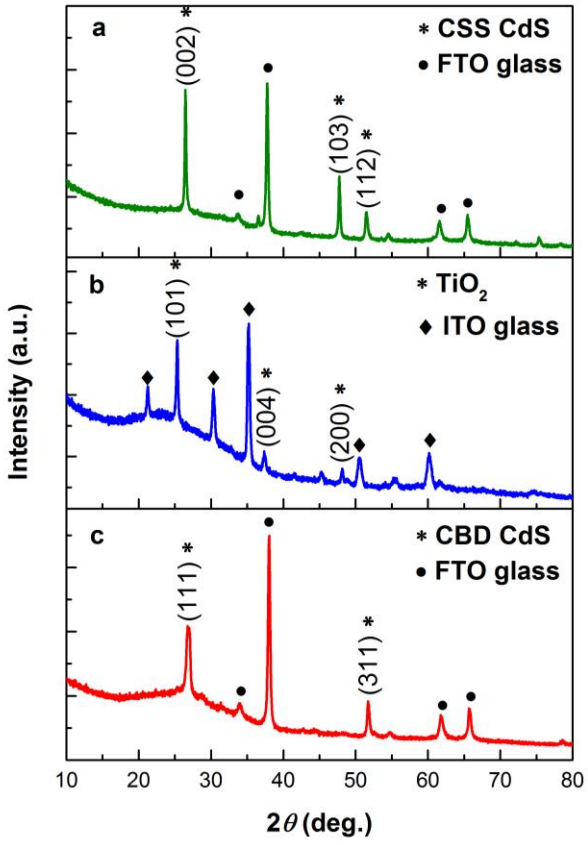

Fig. 22. Morphology of (a) CSS CdS, (b) TiO_2 and (c) CBD CdS window layers

3.2.3. Effect of different window layers on the Sb_2Se_3 film properties

Figure 23 shows SEM top-view and cross-sectional images of the Sb_2Se_3 films deposited onto three different substrates. Top-view images (Fig. 23a-c) indicate that CSS-CdS/Sb_2Se_3, as shown in Fig. 23a, and TiO_2/Sb_2Se_3, as shown in Fig. 22b, have better film coverage compared to CBD-CdS/Sb_2Se_3, as shown in Fig. 23c. The Sb_2Se_3 film on CBD-CdS substrate accommodates lots of voids that are potentially detrimental to solar cell performance, as demonstrated in Section 3.1.2. For all three structures, grains are irregularly shaped, having round corners and comparable size. Cross-sectional images (Fig. 23d-f) reveal that TiO_2/Sb_2Se_3 film, as shown in Fig. 23e, has thickness of ~4 µm, yielding biggest crystals grains with some even spanning the entire layer. This is considered extremely good for charge transport as it lowers the probability of charge carriers colliding with grain boundaries, thus more carriers can potentially be separated and collected [7] [11] [12] [18].

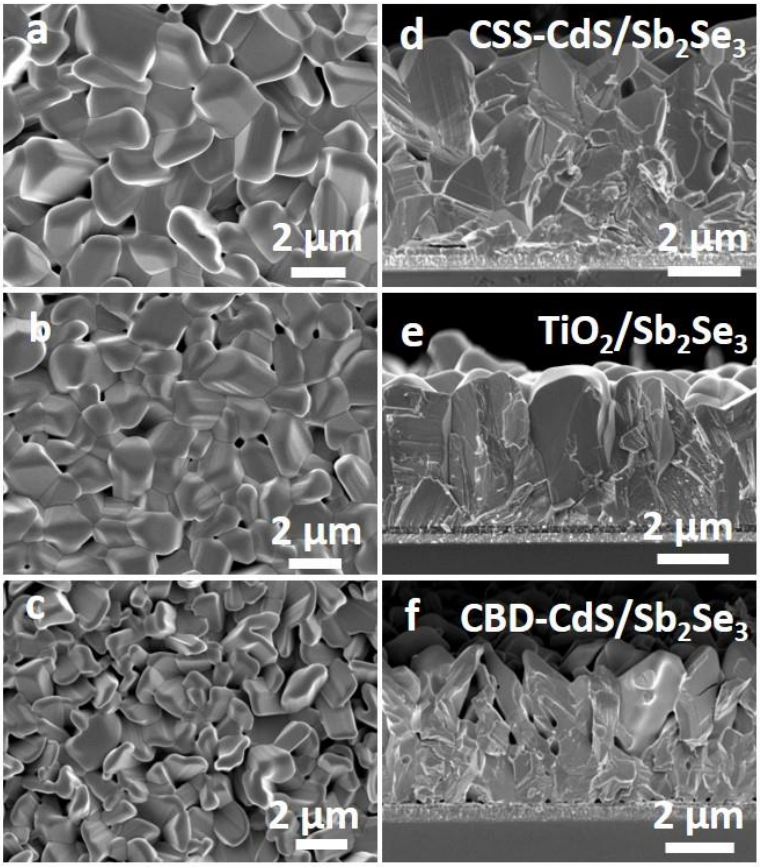

Fig. 23. Morphology of Sb_2Se_3 films deposited onto three different substrates. (a-c) Top-view SEM images with (a) CSS CdS substrate (b) TiO_2 substrate and (c) CBD CdS substrate. (d-f) Cross-sectional SEM mages with (d) CSS CdS substrate (e) TiO_2 substrate and (f) CBD CdS substrate.

Compared with TiO_2/Sb_2Se_3 film, Sb_2Se_3 film on CSS-CdS substrate, as shown in Fig. 23d, has thickness of ~5 µm and yields slightly smaller grains, thus accommodating larger density of grain boundaries. Sb_2Se_3 film on CBD-CdS substrate has thickness of ~5 µm. Crystal structure of CBD-

CdS/Sb_2Se_3, as shown in Fig. 23f, is dispersed and inhomogeneous. Although grains are orientated in the vertical direction, they have wide channels between them, as shown in Fig. 23c. Consequently, this can be attributed to low-temperature deposition of CBD-CdS window layer. Taking a closer look at the interface between CBD-CdS and Sb_2Se_3 layer reveals that there have been certain nucleation sites from which grains have started growing. Surface sites that did not predispose Sb_2Se_3 crystal growth might have left visible voids at the interface. This may imply the surface is rough with step sites, which are at lower surface energy and thereby are more likely to accommodate nucleation of the Sb_2Se_3 crystals [62]. Interfaces of both CSS-CdS/Sb_2Se_3 and TiO_2/Sb_2Se_3 structures suggest the nucleation for the two structures has been more homogenous, resulting in more compact films. Whereas Sb_2Se_3 large grains in CSS-CdS/Sb_2Se_3 film were obtained through applying higher substrate temperature at the deposition, enlarged grains in TiO_2/Sb_2Se_3 are likely to result from post-deposition annealing of TiO_2 window at 450 °C in air, as mentioned in Section 2.2. This significantly improved the nucleation of Sb_2Se_3 atop the TiO_2 film.

XRD diffractograms of the Sb_2Se_3 films deposited onto three different substrates are given in Figure 24. All three films reveal crystal phases characteristic of orthorhombic Sb_2Se_3 crystal structure [13].

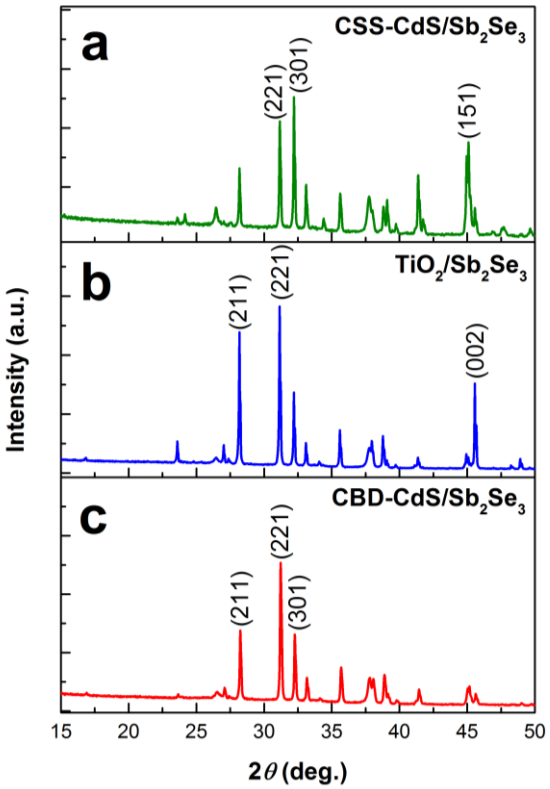

Fig. 24. Morphology of Sb_2Se_3 films grown onto (a) CSS-CdS, (b) TiO_2 and (c) CBD-CdS substrates

What differs is the preference for certain crystal phases. Sb_2Se_3 film atop CSS CdS window layer, as shown in Fig. 24a, reveals that crystal grains are preferably (221)-, (301)- and (501)-orientated. Preferred crystal phases of the Sb_2Se_3 film on the TiO_2 substrate are (211), (221) and (002), as shown in Fig. 24b, which show best correspondence to Sb_2Se_3 films employed in solar cells with record efficiencies [11] [12] [18] . Fig. 24c reveals that the Sb_2Se_3 film grown on the CBD CdS substrate has main crystal phases of (221), (221), (301). Revealed crystal phases show the grains are tilted in all three structures, evidenced by the presence of (*h k 1*) crystal phases, which in theory should facilitate charge transport across the film [13] [17] [19].

3.2.4 Effect of different window layers on Sb_2Se_3 solar cell performance

Figure 25 shows current-voltage (J-V) characteristics of all three solar cells. Main photovoltaic parameters are listed in Table 3. J-V curves demonstrate that the best-performing device is TiO_2/Sb_2Se_3 solar cell with PCE of 3.3%, followed by CSS-CdS/Sb_2Se_3 and CBD-CdS/Sb_2Se_3 solar cells. Solar cell employing TiO_2 window layer produces largest values of V_{OC}, J_{SC}, FF and ultimately PCE, as seen in Table 3. Its open circuit voltage V_{OC} of 0.38 V is comparable to 0.45 V demonstrated by the record device of the same configuration [18]. However, short circuit current J_{SC} of 21.4 mA cm^{-2} is clearly lower than 25.4 mA cm^{-2} produced by the best device [18]. Also, obtained FF of 40.1% is worse than the previously reported FF of 49% [18]. Both lower J_{SC} and FF may be attributed to the quality of the absorber layer. In the 5.5%-efficient TiO_2/Sb_2Se_3 device, absorber layer thickness was smaller (~3 μm) and the grains spanned the entire layer with no apparent grain boundaries [18]. This suggests the absorber had smaller number of grain boundaries, which potentially reduced recombination, hence improving charge collection and decreasing series resistance. CSS-CdS/Sb_2Se_3 produced V_{OC} of 0.38 V that is comparable to 0.42 V achieved by the record device of the same configuration [12]. Obtained J_{SC} of 20.0 mA cm^{-2} is slightly lower than the J_{SC} of TiO_2/Sb_2Se_3 solar cell, but compared with the best literature value, J_{SC} is lower by factor of 1.5 [12]. FF value of 31.7% makes a striking contrast with the literature FF value of 60.4% [12]. Overall, CSS-CdS/Sb_2Se_3 attained efficiency of 2.3%. CBD-CdS/Sb_2Se_3 produced lowest V_{OC} of 0.32 V and lowest J_{SC} of 15.0 mA cm^{-2}. Although its FF of 35.1% was higher than that of CSS-CdS/Sb_2Se_3, the device resulted in having the lowest PCE of 1.7%.

Table 3. Photovoltaic parameters of CBD-CdS/Sb_2Se_3, TiO_2/Sb_2Se_3 and CSS-CdS/Sb_2Se_3solar cells

Device	V_{OC} (V)	J_{SC} (mA cm^{-2})	FF (%)	PCE (%)
CBD-CdS/Sb_2Se_3	0.32	15.0	35.1	1.7
TiO_2/Sb_2Se_3	**0.38**	**21.4**	**40.1**	**3.3**
CSS-CdS/Sb_2Se_3	0.36	20.0	31.7	2.3

Now, it is worth noting that the record 7.6%-efficient superstrate and 9.2%-efficient substrate solar cells have both employed CdS window layer that was deposited by chemical bath deposition [12][13]. Moreover, Shiel et al. have demonstrated that CdS/Sb_2Se_3 band alignments at the interface are superior to TiO_2/Sb_2Se_3, being near optimal for charge transfer [68]. Considering this and the fact that the resistivity of CBD CdS was by far the smallest, CBD-CdS/Sb_2Se_3 solar cell should have performed at least better than the CSS-CdS/Sb_2Se_3 device. This can be partly explained through the obtained results and observations made at the time of the experiments. First and foremost, low performance resulted from clearly very low quality of the Sb_2Se_3 film. As seen in Fig. 23f, established channels and voids, especially at the interface, provided shunting pathways as well as high density of grain boundaries. This hindered the establishment of depletion region and surely increased interfacial and surface recombination, thus hindering charge separation. Second, CBD CdS did not undergo chemical treatment by $CdCl_2$, which has been shown to decrease series resistance and increase shunt resistance [16]. Furthermore, it improves ideality factor, thus facilitating a rectifying p-n junction [7]. Third, the CBD CdS window layer was of low quality. Inhomogeneous film with numerous pinholes proved detrimental to the junction formation at the CBD-CdS/Sb_2Se_3 interface.

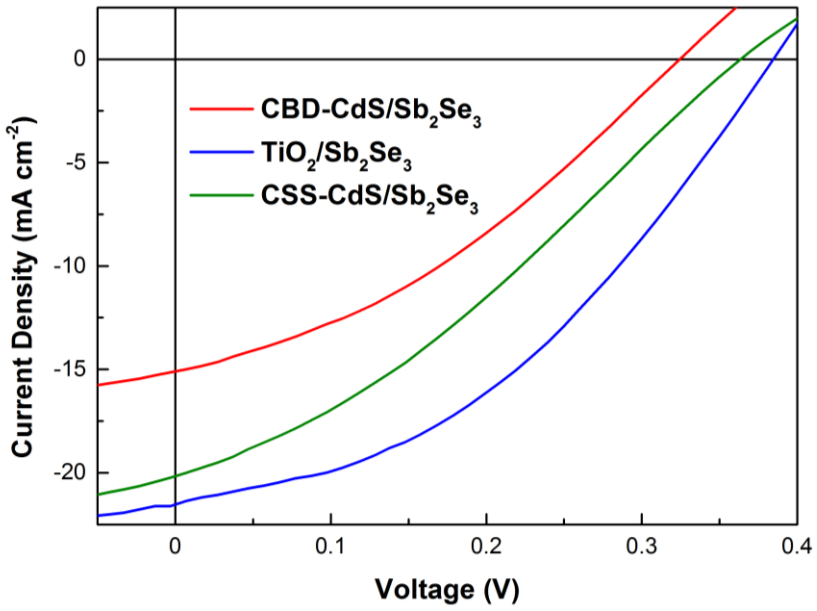

Fig. 25. Current-voltage (J-V) characteristics of CBD-CdS/Sb_2Se_3, TiO_2/Sb_2Se_3 and CSS-CdS/Sb_2Se_3 solar cells

Furthermore, large surface roughness resulted in partial nucleation at the step sites of lower surface energy. Insufficient coverage hampered the formation of depletion region, thus losing carriers to surface recombination. Fourth, CBD CdS window layer, which was deposited at low temperature, was later heated up to 450 °C and exposed to Sb and Se vapour particles. This may have caused intermixing at the interface, where Cd diffused into Sb_2Se_3 film and Se into CdS film,

eventually forming an interfacial CdSe film. This has already been demonstrated in the CSS-CdS/Sb_2Se_3 solar cell [18]. Whilst Wen et al. found it potentially beneficial for the device performance as it can reduce interfacial lattice mismatch and defects [12], Phillips et al. showed that CdSe introduces a potential barrier that impedes charge transport [18]. Fifth, previous studies have shown that the chemically deposited CdS film incorporates $[OH]^-$ defects that stem from the precursor solution, which is believed to obstruct the subsequent film growth and the formation of depletion region [25] [26].

Although both TiO_2 and CSS-CdS window layers were very resistive, as seen in Table 2, their deployment resulted in working PV devices. However, the difference in the resistivity values may explain the difference in the final PV performance. Not only does the large resistivity impede charge transport, but it also affects the position and width of the depletion region [7]. In case of CSS-CdS/Sb_2Se_3, resistivity was even larger than that of the Sb_2Se_3 absorber, hence it is likely the depletion region edge extended into the window layer. This infers that the interfacial defect states are located within the depletion region and thereby act as very potent recombination centres [7]. Furthermore, intermixing may have resulted in potential barrier obstructing charge transport. As for TiO_2/Sb_2Se_3, resistivity was larger than that of Sb_2Se_3 absorber by one order of magnitude, which is also not ideal. Nevertheless, it is likely to have created depletion region that extends rather into the absorber layer, compared with CSS-CdS/Sb_2Se_3. In addition, chemical stability of TiO_2 seemed to have avoided intermixing at the interface, thus post-deposition annealing, as mentioned in Section 2.2, might have helped terminate interface defect states. Lastly, all three J-V curves experienced saturation of photocurrent at 0.5 V bias, which is explained through three interacting effects: first, low concentration of p-type dopants, which are the antimony vacancy (V_{Sb}) and selenium antisite defect (Se_{Sb}), second, surface defect states at the back contact, and third, the Schottky barrier between Sb_2Se_3 and the Au back contact [10] [12] [69].

Figure 26 displays respective EQE and normalised EQE of all three solar cells. Both EQE curves reveal that TiO_2/Sb_2Se_3 solar cell performed the best owing to the broad absorption range of 370-880 nm throughout which EQE was between 70 to 80%. TiO_2/Sb_2Se_3 solar cell also makes a striking contrast with CSS-CdS/Sb_2Se_3 and CBD-CdS/Sb_2Se_3 solar cells at shorter wavelengths of 400-600 nm. That is clearly related to TiO_2 exhibiting larger optical band gap of 3.4 eV, as seen in Figure 21b, which has superb correspondence to the obtained absorption edge, as seen in Fig. 26. In addition, EQE curve of TiO_2/Sb_2Se_3 solar cell bears very close resemblance to the EQE of record TiO_2/Sb_2Se_3 PV device [18]. This demonstrates the viability of the TiO_2 window partnering the Sb_2Se_3 absorber. Provided that the resistivities of both layers are reduced, the PV performance can be further improved. Phillips et al. presumed that the CSS-deposited Sb_2Se_3 layer has Se-rich phases, which

add additional resistance and shunting pathways [18]. Better PV performance of TiO_2/Sb_2Se_3, however, seems to be the consequence of reduced interfacial recombination [18]. CSS-CdS/Sb_2Se_3 solar cell EQE exceeds 90% at ~700 nm, as seen in Fig. 26, but otherwise shows steep declines at both shorter and longer wavelengths. Although the CSS CdS band gap of 2.5 eV suggests the absorption edge should be around 500 nm, EQE is still relatively low between 500 and 600 nm. This may be attributed to the depletion region extending into CdS layer, hence introducing interfacial defect states to the intrinsic layer. CSS-CdS/Sb_2Se_3 also undergoes gradual decline from 700 nm onwards. Remarkably, it coincides with the band gap of the interfacial CdSe film, which can form as the result of intermixing. Phillips et al. showed that low external quantum efficiency in the region between 700 and 1050 nm is due to CdSe layer implying a limiting conduction-band offset, hence impeding charge transport between CSS-CdS and Sb_2Se_3 layer [18]. This also explains, why the EQE of CSS-CdS/Sb_2Se_3 device falls below CBD-CdS/Sb_2Se_3 device. Higher EQE at longer wavelengths implies that the intermixing at the interface of CBD-CdS and Sb_2Se_3 is less pronounced, as seen in Fig. 26. At the same time, EQE of CBD-CdS/Sb_2Se_3 exceeds 70% only in the region between 700 and 970 nm. Lowest EQE in the region between 500 and 700 nm can be again attributed to incomplete coverage of Sb_2Se_3 film, high density of interfacial defect states and large number of potential shunting pathways. At shorter wavelengths (<500 nm) carriers are lost to parasitic absorption by the CdS window layer [18]. Normalised external quantum efficiency exemplifies very well how TiO_2/Sb_2Se_3 attained the highest efficiency. Exhibiting successful photocarrier generation and extraction in the broadest wavelength region affirmed the compatibility of TiO_2 partnering Sb_2Se_3 in a solar cell configuration.

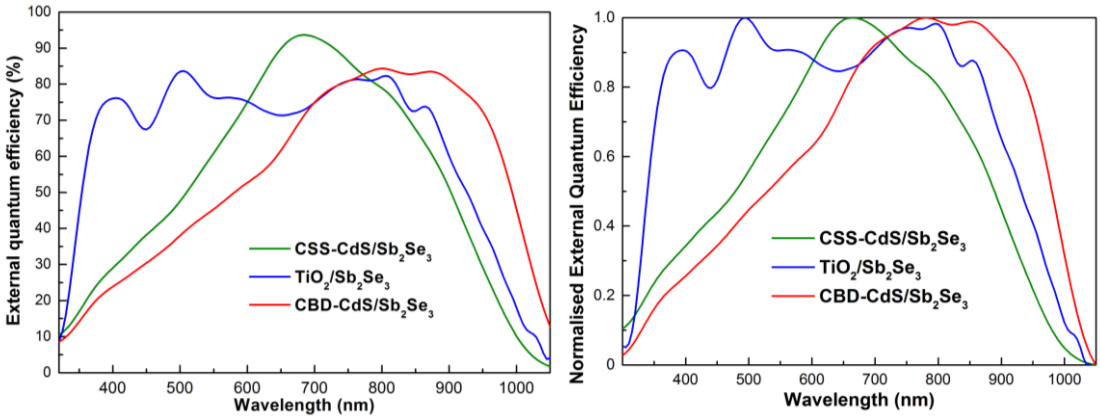

Fig. 26. EQE and normalised EQE of CSS CdS/Sb_2Se_3, TiO_2/Sb_2Se_3 and CBD CdS/Sb_2Se_3 solar cells

CONCLUSIONS

This study was based on fabricating Sb_2Se_3 thin films and Sb_2Se_3 solar cells by close-spaced sublimation technique. The study included gaining broader understanding of the underlying principles of solar cells, acquiring experience with ultrasonic spray pyrolysis and chemical bath deposition techniques, post-deposition treatment techniques, materials characterisation and device characterisation. As a result, a systematic study was carried out to investigate (1) the effect of substrate temperature on the Sb_2Se_3 thin film properties and the Sb_2Se_3 solar cell performance and (2) the effect of different window layers on the Sb_2Se_3 thin film properties and the Sb_2Se_3 solar cell performance. This involved analysing the physicochemical processes within the film at the time of deposition, and the morphological changes deposited films went through, when using different substrate temperatures and different substrates. Furthermore, the Sb_2Se_3 solar cells were assessed in relation with the crystal structure of the deposited Sb_2Se_3 film. The results are as follows:

1. The structural and morphological properties of the Sb_2Se_3 films revealed strong dependence upon the substrate temperature set during the deposition of close-spaced sublimation. Crystal growth regarding the grain size and structure density varied at different substrate temperatures of 300 to 450 $^{\circ}$C and was explained through crystal growth theory comprising nucleation, surface diffusion and coalescence.

2. Photovoltaic performance of the Sb_2Se_3 solar cells was also in correlation with the substrate temperature. Increasing substrate temperature resulted in the Sb_2Se_3 solar cells with superior performance. Solar cells employing the Sb_2Se_3 films deposited at 300 and 350 $^{\circ}$C did not function, whereas utilising the Sb_2Se_3 films deposited at 400 and 450 $^{\circ}$C produced solar cells with PCE of 1.6% and 2.3%, respectively. Thus, substrate temperature of 450 $^{\circ}$C was regarded as optimal.

3. Superior solar cell performance was attributed to better Sb_2Se_3 film quality at the substrate temperature of 450 $^{\circ}$C. Higher temperature increased coalescence rate, eventually providing denser structure with less voids, larger grains and smaller density of grain boundaries. This was evidenced by Sb_2Se_3-450 $^{\circ}$C solar cell clearly having larger EQE over a broad region of 350 to 900 nm, compared to the Sb_2Se_3-400 $^{\circ}$C solar cell.

4. Window layers, onto which the Sb_2Se_3 were grown, showed distinct optoelectronic and structural properties. CBD CdS film showed resistivity of 100 Ω·cm that was three orders of magnitude smaller than that of CSS CdS and TiO_2 (>10^5 Ω·cm). CBD CdS and CSS CdS films revealed cubic and hexagonal crystal structures, respectively. Yet both had equal band gap of 2.4 eV. TiO_2 film had band gap of

3.4 eV and exhibited mainly amorphous crystal structure with small concentration of anatase crystal phase.

5. The Sb_2Se_3 crystal growth was clearly dependent on the respective window layer. Sb_2Se_3 film on the TiO_2 substrate gave the densest structure with least voids, largest grains and smallest density of grain boundaries. This was attributed to the chemical stability and reduced number of surface defect states at the interface, improved by post-deposition annealing. In comparison, Sb_2Se_3 film on the CSS CdS substrate had slightly bigger voids and smaller grains, thus having larger density of grain boundaries. Sb_2Se_3 film on the CBD CdS substrate was of lowest quality with dispersed structure, large voids and thin elongated grains. This was attributed to the CdS window layer that in turn suffered from low quality, as it incorporated visible pinholes and step sites that might have driven the Sb_2Se_3 nucleation.

6. Changing window layer did affect the Sb_2Se_3 solar cell performance. TiO_2/Sb_2Se_3 solar cell attained largest J_{SC}, V_{OC}, and FF, ultimately resulting in PCE of 3.3%. Highest performance was attributed to the highest absorber quality and consolidated junction. CSS-CdS/Sb_2Se_3 solar cell produced PCE of 2.3%. Despite showing relatively large grains and dense structure, CSS CdS facilitated intermixing at the CSS-CdS/Sb_2Se_3 interface, thereby introducing a electrostatic potential barrier that hindered charge transport. In addition, CSS CdS showed largest resistivity, which alluded to poor junction formation and higher series resistance. CBD-CdS/Sb_2Se_3 solar cell achieved PCE of 1.7%, which was attributed to low quality of window and the absorber. Despite showing by far the lowest resistivity, this did not translate into higher performance.

7. Best-performing TiO_2/Sb_2Se_3 solar cell showed consistent EQE of over 70% over a broad region of 370 to 880 nm. It made a striking contrast with CdS window layers in the region between 370 and 660 m, which was attributed to increased light transmission, owing to larger band gap of TiO_2. CSS CdS had the second largest EQE but had steep declines both at shorter and longer wavelengths. Reduced EQE at longer wavelengths was attributed to CdSe interface layer, which was not seen in CBD-CdS/Sb_2Se_3. CBD-CdS/Sb_2Se_3 was largest at longer wavelengths but showed lowest EQE at shorter wavelengths, which could be explained through parasitic absorption, abundant surface recombination and presence of shunting pathways.

SUMMARY

Photovoltaics (PV) is one of the key renewable technologies to help fulfil increasing global energy demand and tackle global warming. At the same time, comprehensive utilisation requires addition of new cost-effective solar PV technologies that produce high photoconversion efficiency (PCE). Sb_2Se_3 is a promising photovoltaic absorber that could be employed in thin film solar cells. It is abundant and low-toxicity compound. Single orthorhombic phase, high vapour pressure and low melting point allows the deposition of Sb_2Se_3 absorbers by close-spaced sublimation, which has been previously deployed to fabricate CdTE solar cells. So far, champion Sb_2Se_3 solar cells have been fabricated by either rapid thermal evaporation (RTE), vapour transport deposition (VTD) or close-spaced sublimation (CSS).

This study focused on the development of Sb_2Se_3 thin film solar cells by close-spaced sublimation. This included the investigation into (1) the effect of substrate temperature on the Sb_2Se_3 thin film properties and the Sb_2Se_3 solar cell performance and (2) the effect of different window layers on the Sb_2Se_3 thin film properties and the Sb_2Se_3 solar cell performance.

Optimal substrate temperature was determined through depositing Sb_2Se_3 films at different substrate temperatures of 300 to 450 $^{\circ}$C by close-spaced sublimation. It transpired that the highest substrate temperature of 450 $^{\circ}$C at the CSS deposition produced the most compact Sb_2Se_3 film with largest crystal grains, least voids and lowest density of grain boundaries. We attributed this to higher substrate temperature, which lowered nucleation density, but increased the coalescence rate of grains through increased adatom mobility. Sb_2Se_3 solar cell performance also correlated with the substrate temperature. Substrate temperatures of 300 and 350 $^{\circ}$C did not give working photovoltaic devices. On the contrary, Sb_2Se_3 films deposited at substrate temperatures of 400 and 450 $^{\circ}$C were employed in solar cells that attained PCE of 1.6% and 2.3%, respectively. Consequently, the substrate temperature of 450 $^{\circ}$C was found optimal for Sb_2Se_3 film deposition.

The effect of different window layers on the Sb_2Se_3 film properties and the Sb_2Se_3 solar cell performance was studied by partnering Sb_2Se_3 absorber layer with CdS and TiO_2 window layers, deposited by chemical bath deposition (CBD CSS) and ultrasonic spray pyrolysis, respectively. Previously achieved 2.3%-efficient solar cell employed CdS, which was deposited by close-spaced sublimation (CSS CdS). The Sb_2Se_3 film grown onto TiO_2 substrate produced the densest structure with deposited grains almost spanning the entire absorber layer. TiO_2/Sb_2Se_3 solar cell thus produced highest PCE of 3.3%, followed by CSS-CdS/CSS CdS and CBD-CdS/Sb_2Se_3 solar cells with PCE of 2.3% and 1.7%, respectively.

REFERENCES

[1] 2019 United Nations Framework Convention on Climate Change, “The Paris Agreement,” 22 October 2018. [Online]. Available: https://unfccc.int/process-and-meetings/the-paris-agreement/the-paris-agreement. [Accessed 2 May 2019].

[2] IRENA, “Global energy transformation: The REmap transition pathway (Background to report to 2019 edition),” International Renewable Energy Agency, Abu Dhabi, 2019.

[3] International Energy Agency, “Renewables 2018, Analysis and Forecasts to 2023 (Executive Summary),” IEA Publications, France, 2018.

[4] L. Hook, “Solar energy: panel engineers move over to the dark side,” *Financial Times,* 12 March 2019.

[5] H. A. Atwater and A. Polman, “Plasmonics for improved photovoltaic devices,” *Nature Materials,* 9, 3, 205-213, 2010.

[6] T. D. Lee and A. U. Ebong, “A review of thin film solar cell technologies and challenges,” *Renewable and Sustainable Energy Reviews,* 70, 1286–1297, 2017.

[7] J. . Nelson, The Physics of Solar Cells, ed., Imperial College Press, 2003, .

[8] ITRPV, “International Technology Roadmap for Photovoltaic (ITRPV) 2018 Results,” ITRPV, Frankfurt am Main, 2019.

[9] X. Liu, J. Chen, M. Luo, M. Leng, Z. Xia, Y. Zhou, S. Qin, D.-J. Xue, L. Lv, H. Huang, D. Niu and J. Tang, “Thermal Evaporation and Characterization of Sb2Se3 Thin Film for Substrate Sb2Se3/CdS Solar Cells,” *ACS Applied Materials & Interfaces,* 6, 13, 10687–10695, 2014.

[10] N. Spalatu, Development of CdTe Absorber Layer for Thin-Film Solar Cells, Tallinn: TUT Press, 2017.

[11] O. S. Hutter, L. J. Phillips, K. Durose and J. D. Major, “6.6% efficient antimony selenide solar cells using grain structure control and an organic contact layer,” *Solar Energy Materials and Solar Cells,* 188, 177-181, 2018.

[12] X. Wen, C. Chen, S. Lu, K. Li, R. Kondrotas, Y. Zhao, W. Chen, L. Gao, C. Wang, J. Zhang, G. Niu and J. Tang, “Vapor transport deposition of antimony selenide thin film solar cells with 7.6% efficiency,” *Nature Communications,* 9, 2041–1723, 2179, 2018.

[13] Z. Li, X. Liang, G. Li, H. Liu, H. Zhang, J. Guo, J. Chen, K. Shen, X. San, W. Yu, R. E. I. Schropp and Y. Mai, “9.2%-efficient core-shell structured antimony selenide nanorod array solar cells,” *Nature Communications,* 10, 25, 2019.

[14] Y. Zhou, M. Leng, Z. Xia, J. Zhong, H. Song, X. Liu, B. Yang, J. Zhang, J. Chen, K. Zhou, J. Han, Y. Cheng and J. Tang, “Solution-Processed Antimony Selenide Heterojunction Solar Cells,” *Advanced Energy Materials,* 4, 8, 1301846, 2014.

[15] G. Ghosh, “The Sb-Se (Antimony-Selenium system),” *Journal of Phase Equilibria,* 14, 6, 753–763, 1993.

[16] L. Wang, M. Luo, S. Qin, X. Liu, J. Chen, B. Yang, M. Leng, D.-J. Xue, Y. Zhou, L. Gao, H. Song and J. Tang, “Ambient CdCl2 Treatment on CdS Buffer Layer for Improved Performance of Sb2Se3 Thin Film Photovoltaics,” *Applied Physics Letters,* 107, 4, 143902, 2015.

[17] Y. Zhou, L. Wang, S. Chen, S. Qin, X. Liu, J. Chen, D.-J. Xue, M. Luo, Y. Cao, Y. Cheng, E. H. Sargent and J. Tang, “Thin-film Sb2Se3 photovoltaics with oriented one-dimensional ribbons and benign grain boundaries,” *Nature Photonics,* 9, 6, 409–415, 2015.

[18] L. J. Phillips, C. N. Savory, O. S. Hutter, P. J. Yates, H. Shiel, S. Mariotti, L. Bowen, M. Birkett, K. Durose, D. O. Scanlon and J. D. Major, “Current Enhancement via a TiO2 Window Layer for CSS Sb2Se3 Solar Cells: Performance Limits and High Voc,” *IEEE Journal of Photovoltaics,* 9, 2, 544–551, 2019.

[19] C. Chen, D. C. Bobela, Y. Yang, S. Lu, K. Zeng, C. Ge, B. Yang, L. Gao, Y. Zhao, M. C. Beard and J. Tang, "Characterization of basic physical properties of Sb2Se3 and its relevance for photovoltaics," *Frontiers of Optoelectronics,* 10, 1, 18–30, 2017.

[20] S. Messina, M. T. S. Nair and P. K. Nair, "Antimony Selenide Absorber Thin Films in All-Chemically Deposited Solar Cells," *Journal of The Electrochemical Society,* 156, 5, H327, 2009.

[21] Y. C. Choi, T. N. Mandal, W. S. Yang, Y. H. Lee, S. H. Im, J. H. Noh and S. I. Seok, "Sb2Se3-Sensitized Inorganic-Organic Heterojunction Solar Cells Fabricated Using a Single-Source Precursor," *Angewandte Chemie International Edition,* 53, 5, 1329–1333, 2013.

[22] L. Wang, D.-B. Li, K. Li, C. Chen, H.-X. Deng, L. Gao, Y. Zhao, F. Jiang, L. Li, F. Huang, Y. He, H. Song, G. Niu and J. Tang, "Stable 6%-efficient Sb2Se3 solar cells with a ZnO buffer layer," *Nature Energy,* 2, 4, 2017.

[23] C. Chen, L. Wang, L. Gao, D. Nam, D. Li, K. Li, Y. Zhao, C. Ge and H. L. H. S. J. T. Hyeonsik Cheong, "6.5% Certified Efficiency Sb2Se3 Solar Cells Using PbS Colloidal Quantum Dot Film as Hole-Transporting Layer," *ACS Energy Letters,* 2, 9, 2125–2132, 2017.

[24] L. Guo, B. Zhang, Y. Qin, D. Li, L. Li, X. Qian and F. Yan, "Tunable Quasi-One-Dimensional Ribbon Enhanced Light Absorption in Sb2Se3 Thin-film Solar Cells Grown by Close-Space Sublimation," *Solar RRL,* 2, 10, 1800128, 2018.

[25] M. Üürike, Influence of pH on the properties of chemically deposited CdS thin films and solar cells, Tallinn: TUT Press, 2017.

[26] N. Maticiuc, Mechanism of Changes in the Properties of Chemically Deposited CdS Thin Films Induced by Thermal Annealing, Tallinn: TUT Press, 2015.

[27] L. Li, S. Yang, F. Han, L. Wang, X. Zhang, Z. Jiang and A. Pan, "Optical Sensor Based on a Single CdS Nanobelt," *Sensors,* 14, 4, 7332–7341, 2014.

[28] J. Zhao, J. A. Bardecker, A. M. Munro, M. S. Liu, Y. Niu, I.-K. Ding, J. Luo, B. Chen, A. K.-Y. Jen and D. S. Ginger, "Efficient CdSe/CdS Quantum Dot Light-Emitting Diodes Using a Thermally Polymerized Hole Transport Layer," *Nano Letters,* 6, 3, 463–467, 2006.

[29] A. L. Salas-Villasenor, I. Mejia, M. Sotelo-Lerma, Z. B. Guo, H. N. Alshareef and M. A. Quevedo-Lopez, "Improved electrical stability of CdS thin film transistors through hydrogen-based thermal treatments," *Semiconductor Science and Technology,* 29, 8, 085001, 2014.

[30] V. C. Anitha, A. N. Banerjee and S. W. Joo, "Recent developments in TiO2 as n- and p-type transparent semiconductors: synthesis, modification, properties, and energy-related applications," *Journal of Materials Science,* 50, 23, 7495–7536, 2015.

[31] D. A. H. Hanaor and C. C. Sorrell, "Review of the anatase to rutile phase transformation," *Journal of Materials Science,* 46, 4, 855–874, 2010.

[32] E. Kärber, A. Katerski, I. O. Acik, A. Mere, V. Mikli and M. Krunks, "Sb2S3 grown by ultrasonic spray pyrolysis and its application in a hybrid solar cell," *Beilstein Journal of Nanotechnology,* 7, 1662–1673, 2016.

[33] P. Cui, D. Wei, J. Ji, H. Huang, E. Jia, S. Dou, T. Wang, W. Wang and M. Li}, "Planar p-n homojunction perovskite solar cells with efficiency exceeding 21.3%," *Nature Energy,* 4, 2, 150-159, 2019.

[34] U. Bach, D. Lupo, P. Comte, E. Moser, F. Weissörtel, J. Salbeck, H. Spreitzer and M. Grätzel, "Solid-state dye-sensitized mesoporous TiO2 solar cells with high photon-to-electron conversion efficiencies," *Nature,* 395, 6702, 583–585, 1998.

[35] E. H. Jung, N. J. Jeon, E. Y. Park, C. S. Moon, T. J. Shin, T.-Y. Yang, J. H. Noh and J. Seo, "Efficient, stable and scalable perovskite solar cells using poly(3-hexylthiophene)," *Nature,* 567, 7749, 511–515, 2019.

[36] Y. Lu, W.-J. Yin, K.-L. Peng, K. W. a. Q. Hu, A. Selloni, F.-R. Chen, L.-M. Liu and M.-L. Sui, "Self-hydrogenated shell promoting photocatalytic H2 evolution on anatase TiO2," *Nature Communications,* 9, 1, 2018.

[37] Y. Wang, L. Liu, C. Meng, Y. Zhou, Z. Gao, X. Li, X. Cao, L. Xu and W. Zhu, "A novel ethanol gas sensor based on TiO2/Ag0.35V2O5 branched nanoheterostructures," *Scientific Reports,* 6, 1, 2016.

[38] L. Li, P. Zhang, W.-M. Wang, H. Lin, A. B. Zerdoum, S. J. Geiger, Y. Liu, N. Xiao, Y. Zou, O. Ogbuu, Q. Du, X. Jia, J. Li and J. Hu, "Foldable and Cytocompatible Sol-gel TiO2 Photonics," *Scientific Reports,* 5, 1, 2015.

[39] I. Dundar, M. Krichevskaya, A. Katerski and I. O. Acik, "TiO2 thin films by ultrasonic spray pyrolysis as photocatalytic material for air purification," *Royal Society Open Science,* 6, 2, 181578, 2019.

[40] L. Kranz, C. Gretener, J. Perrenoud, R. Schmitt, F. Pianezzi, F. L. Mattina, P. Blösch, E. Cheah, A. Chirilua, C. M. Fella, H. Hagendorfer, T. Jäger, S. Nishiwaki, A. R. U, S. B and A. N. T, "Doping of polycrystalline CdTe for high-efficiency solar cells on flexible metal foil," *Nature Communications,* 4, 1, 2013.

[41] U. Mishra and J. Singh, Semiconductor Device Physics and Design, Dordrecht: Springer, 2007.

[42] J. Poortmans, Thin Film Solar Cells, Wiley-Blackwell, 2006.

[43] B. Bharti, S. Kumar, H.-N. Lee and R. Kumar, "Formation of oxygen vacancies and Ti3+ state in TiO2 thin film and enhanced optical properties by air plasma treatment," *Scientific Reports,* 6, 1, 2016.

[44] S. M. Sze and K. K. Ng, Physics of Semiconductor Devices, Wiley, 2006.

[45] P. Würfel, Physics of Solar Cells, Weinheim: Wiley, 2005.

[46] J. S. Eensalu, A. Katerski, E. Kärber, I. O. Acik, A. Mere and M. Krunks, "Uniform Sb2S3 optical coatings by chemical spray method," *Beilstein Journal of Nanotechnology,* 10, 198–210, 2019.

[47] J. S. Eensalu, M. Krunks, I. Gromyko, A. Katerski and A. Mere, "A comparative study on physical properties of Al-doped zinc oxide thin films deposited from zinc acetate and zinc acetylacetonate by spray pyrolysis," *Energetika,* 63, 2, 2017.

[48] M. F. García-Sánchez, J. Peña, A. Ortiz, G. Santana, J. Fandino, M. Bizarro, F. Cruzgandarilla and J. Alonso, "Nanostructured YSZ thin films for solid oxide fuel," *Solid State Ionics,* 179, 7–8, 243-249, 2008.

[49] J. S. Eensalu, Keemilise pihustamise meetoditel sadestatud ZnO:Al õhukeste kilede uurimine, Tallinn: TUT Press, 2017.

[50] L. Filipovic, S. Selberherr, G. C. Mutinati, E. Brunet, S. Steinhauer, A. Köck, J. Teva, J. Kraft, J. Siegert and F. Schrank, "Modeling spray pyrolysis deposition," in *Lecture Notes in Engineering and Computer Science*, 2, 2013, 987–992.

[51] Z. Chen, TiO2 thin films by ultrasonic spray pyrolysis., Tallinn: TUT Press, 2018.

[52] R. Suresh, V. Ponnuswamy and R. Mariappan, "Effect of solvent and substrate temperature on morphology of cerium oxide thin films by simple nebuliser spray pyrolysis technique," *Materials Technology,* 30, 1, 12–22, 2014.

[53] P. E. Flewitt and R. Wild, Physical Methods for Materials Characterisation, Taylor & Francis, 1994.

[54] P. W. Hawkes and J. C. H. Spence, Science of Microscopy, New York: Springer, 2007.

[55] B. D. Fahlman, Materials Chemistry, Springer Netherlands, 2011.

[56] “SEM scheme [Digital image],” University of Cambridge, [Online]. Available: https://www.eng-atoms.msm.cam.ac.uk/Images/SEMScheme/image_view_fullscreen.

[57] R. Krautmann, TiO2 maatriksist ja kulla nanoosakestest koosnev nanostruktuur valguse neelduvuse suurendamiseks kilepäikesepaneelides, Tartu: Tartu Ülikool, 2016.

[58] D. Halliday, R. Resnick and J. Walker, Fundamentals of Physics, Wiley, 2013.

[59] M. Alonso and E. Finn, Physics, Addison-Wesley, 1992.

[60] R. Rammula, Atomic layer deposition of HfO2 – nucleation, growth and structure development of thin films, Tartu: Tartu Ülikooli Kirjastus, 2011.

[61] L. J. v. d. Pauw, “A Method of Measuring the Resistivity and Hall Coefficient on Lamellae of Arbitrary Shape,” *Philips Research Reports,* 1958.

[62] J. Major, *CdTe solar cells: growth phenomena and device performance,* Durham University: Doctoral thesis, 2008.

[63] H. Khallaf, I. O. Oladeji, G. Chai and L. Chow, “Characterization of CdS thin films grown by chemical bath deposition using four different cadmium sources,” *Thin Solid Films,* vol. 516, 21, 7306–7312, 2008.

[64] C. Dette, M. A. Perez-Osorio, C. S. Kley, P. Punke, C. E. Patrick, P. Jacobson, F. Giustino, S. J. Jung and K. Kern, “TiO2 Anatase with a Bandgap in the Visible Region,” *Nano Letters,* 14, 11, 6533–6538, 2014.

[65] H. He, K. Yang, S. Ren, T. Liu and N. Wang, “Enhanced Photovoltaic Properties of the Solar Cells Based on Cosensitization of CdS and Hydrogenation,” *Journal of Nanomaterials,* 2015, 1–6, 2015.

[66] F. Fazli, M. Ahmad, C. Soon, N. Nafarizal, A. Suriani, A. Mohamed, M. Mamat, M. Malek, M. Shimomura and K. Murakami, “Dye-sensitized solar Cell using pure anatase TiO2 annealed at different temperatures,” *Optik,* 140, 1063–1068, 2017.

[67] N. C. S. Vieira, E. G. R. Fernandes, A. A. A. d. Queiroz, F. E. G. Guimaraes and V. Zucolotto, “Indium tin oxide synthesized by a low cost route as SEGFET pH sensor,” *Materials Research,* 16, 5, 1156–1160, 2013.

[68] H. Shiel, O. S. Hutter, J. E. N. Swallow, L. A. Jones, T. J. Featherstone, M. J. Smiles, P. K. Thakur, L. J. Phillips, K. Durose, J. D. Major, V. R. Dhanak, T.-L. Lee and T. D. Veal, “Band Alignment Measurements of Sb2Se3 Solar Cells Using HAXPES,” 2018. [Online]. Available: https://www.pvsat.org.uk/Files/Other/wr/wed/10%20Shiel.pdf.

[69] T. J. McMahon and A. L. Fahrenbuch, “Insights into the nonideal behavior of CdS/CdTe solar cells.,” in *Conference Record of the 28th IEEE Photovoltaic Specialists Conference*, Anchorage, USA, 2000.